Thermal and Deposition Modeling of the Canister Deposition Field Demonstration

Spent Fuel and Waste Disposition

Prepared for
U.S. Department of Energy
Spent Fuel and Waste Science and Technology

Pacific Northwest National Laboratory

SR Suffield
PJ Jensen
BJ Jensen
R Ekre
JA Fort
WA Perkins
C Grant
BD Hanson
SB Ross

September 3, 2021
M2SF-21PN010208014
PNNL-31882

SUMMARY

This report provides initial thermal and deposition modeling results of the spent nuclear fuel (SNF) storage system planned for use in the Canister Deposition Field Demonstration (CDFD). The goal of the CDFD testing is to collect deposition measurements on the surface of the dry shielded canister (DSC) to aid in chloride-induced stress corrosion crack (CISCC) research. Ideally this testing will occur in a marine coastal environment but at the time of this report no official site has been selected. The CDFD will use the NUHOMS® Advanced Horizontal Storage Module – High Seismic (AHSM-HS) with a 32PTH2 canister. The SNF assemblies will be replaced with electrical heaters. Canisters are currently being outfitted with these heaters and tested at Sandia National Laboratories (SNL). Thermal modeling was conducted to ensure the electrical heaters were representative of the temperature distribution found within a storage system with SNF. Deposition models were built to evaluate contaminant deposition on SNF canisters. The CDFD testing will help to validate these models, which will then be used to plan and inform on-site test programs and predictive models for the timing and occurrence of canister CISCC.

This page is intentionally left blank.

ACKNOWLEDGEMENTS

This work was conducted as part of the U.S. Department of Energy Spent Fuel and Waste Science and Technology campaign. The authors thank Ned Larson of the Department of Energy and Sylvia Saltzstein of Sandia National Laboratories (SNL) for their support and leadership in this research program.

The authors would like to thank Sam Durbin, Eric Lindgren, and Greg Koenig of SNL for the information about their experiment. We would also like to thank Charles Bryan and Rebecca Schaller of SNL for collaborating with us. We appreciate the information sharing provided by all the SNL staff that were involved. Also, we would like to thank Prakash Narayanan and others at Orano for design information to support research related to the Orano TN NUHOMS® 32PTH2 dry shielded canisters (DSCs) and the associated horizontal storage modules.

This page is intentionally left blank.

CONTENTS

FIGURES

TABLES

This page is intentionally left blank.

ACRONYMS

AHSM-HS	Advanced Horizontal Storage Module – High Seismic
CAD	computer-aided design
CDF	cumulative distribution function
CDFD	Canister Deposition Field Demonstration
CE	Combustion Engineering
CFD	computational fluid dynamics
CISCC	chloride-induced stress corrosion crack
DSC	dry shielded canister
FDS	Fire Dynamics Simulator
ISFSI	Independent Spent Fuel Storage Installation
LES	large eddy simulation
MPI	Message Passing Interface
NIST	National Institute of Standards and Technology
NU	Nusselt Number
PHT	peak heater temperature
PNNL	Pacific Northwest National Laboratory
RANS	Reynolds-averaged Navier-Stokes
Re	Reynolds Number
RH	Relative Humidity
SSA	sea-salt aerosols
SCC	stress corrosion cracking
SNF	spent nuclear fuel
SNL	Sandia National Laboratories
SST	shear stress transport
TC	Thermocouple
UFSAR	Updated Final Safety Analysis Report

This page is intentionally left blank.

THERMAL AND DEPOSITION MODELING OF THE CANISTER DEPOSITION FIELD DEMONSTRATION

1. INTRODUCTION

The Canister Deposition Field Demonstration (CDFD) is planned to collect surface deposition measurements over an extended time period on a dual purpose canister to aid chloride-induced stress corrosion crack (CISCC) research. The plan is to conduct the test in a marine coastal environment but at the time of this report no official site has been selected. The CDFD will use the NUHOMS® Advanced Horizontal Storage Module – High Seismic (AHSM-HS) with a 32PTH2 canister. To avoid worker exposure and facilitate surface measurements, the spent nuclear fuel (SNF) assemblies will be replaced with electrical heaters. Multiple storage modules will be included to test multiple decay heat loads. A high heat load, low heat load, and no heat load canister will be incorporated into a connected set of three AHSMs. The no heat load canister will serve as a control, with deposition on this canister mainly driven by wind effects.

Initial thermal and deposition models are presented in this report and model results should be considered as preliminary. Development of these models will continue. The thermal modeling was conducted to ensure the electrical heaters were representative of the thermal environment found within a SNF storage system and to verify that heat flux to the control canister (no heat load) was minimized. The deposition models are built from the thermal models and were constructed to predict the contaminant deposition on SNF canisters. To understand the effects of wind on the storage system, an initial wind effects model and site wide model have also been developed. Since no specific site has been selected, the site model represents a generic location.

Section 2 presents the thermal models and results. Section 3 describes the linkage between the thermal and deposition modeling. Section 4 presents the approach to deposition modeling along with initial results. An example of a site model is also included in this section. Section 5 summarizes the conclusions and recommendations from this work and Section 6 lists the references.

This page is intentionally left blank.

2. THERMAL MODELING

Two model types are described in this section, baseline models and the heater models. A baseline computational fluid dynamics (CFD) model of the 32PTH2 canister in a NUHOMS® AHSM-HS was constructed using the commercial software STAR-CCM+ (Siemens PLM Software 2021). The baseline model included SNF assemblies, which were modeled as single regions within each channel box in the basket. This model will provide baseline temperature profiles which can be compared against the heater assembly model. The baseline model is expanded to a three AHSM-HS model to consider approaches to insulation between modules. An external flow field was added to the baseline model to explore wind effects. In the heater assembly model, the SNF assemblies have been replaced by electrical heaters. The electrical heater parts are modeled in detail. A brief description of the models and preliminary temperature results are given in this section.

2.1 Baseline Model Description

The baseline model of the NUHOMS® AHSM-HS with a 32PTH2 canister included SNF. The SNF assemblies were not modeled in detail but instead represented with a single homogeneous region within the channel box. The AHSM-HS and 32PTH2 canister model is built with information provided by Orano under a non-disclosure agreement. This report will focus more on modeling results than details of model construction to avoid exposing proprietary design information. A general description of the model is presented in this this section.

2.1.1 Geometry and Materials

The geometry for the CFD model was generated using the commercial computer-aided design (CAD) software SolidWorks (Dassault Systemes SolidWorks Corp., 2020). The geometry includes a dry shielded canister (DSC) within a ventilated concrete overpack; more specifically, the AHSM-HS version of the NUHOMS® storage module and the 32PTH2 DSC. The CAD geometry for the NUHOMS® storage module and DSC was constructed from drawings and details provided by Orano. A cross-sectional plot of the CAD geometry is shown in Figure 2-1.

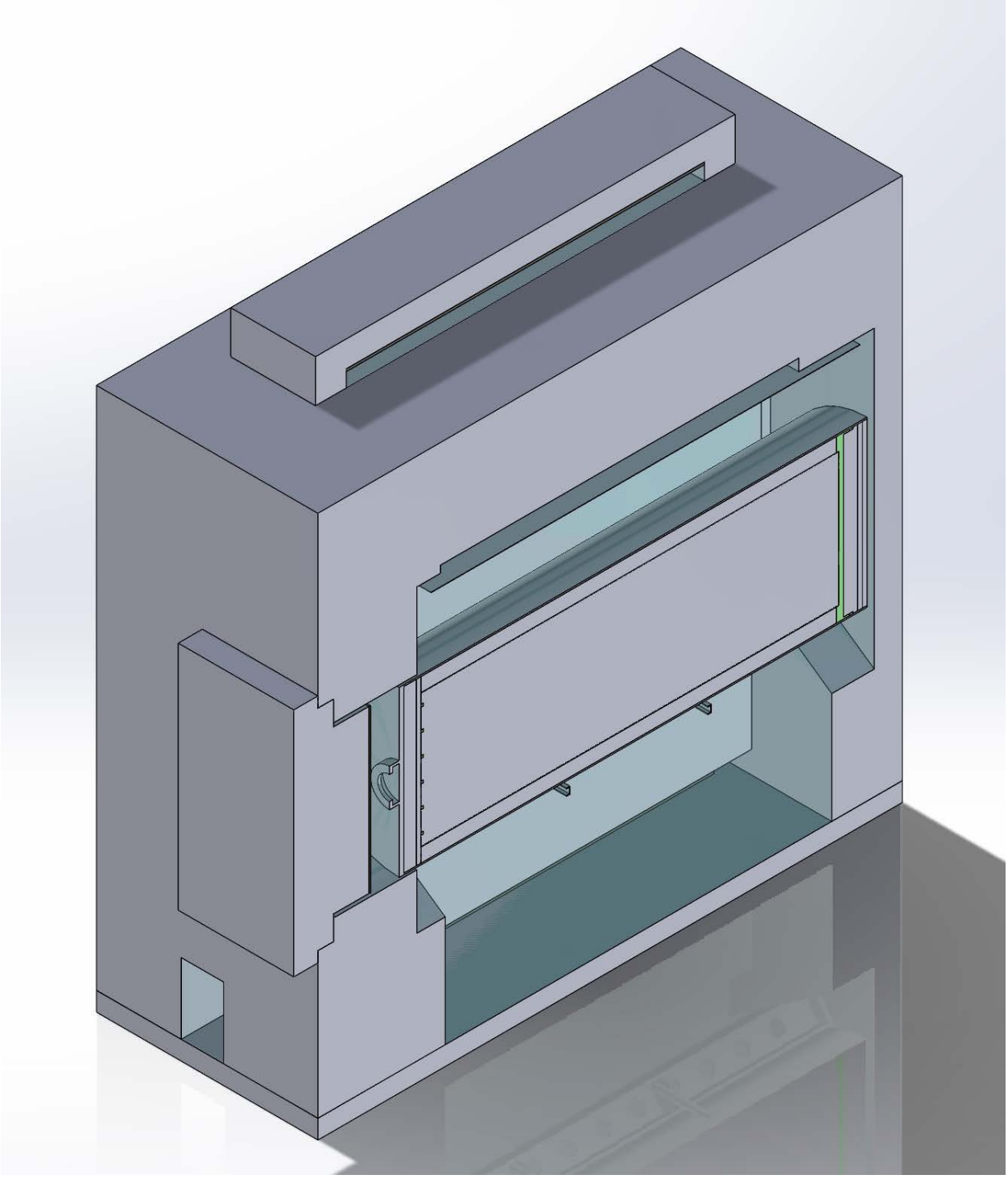

Figure 2-1. Cross-sectional View of AHSM-HS with 32PTH2 Canister CAD Geometry

The baseline model included Combustion Engineering (CE) 16x16 fuel assemblies. These fuel assemblies are not explicitly included in the model and instead modeled as a homogeneous solid region within the channel box. Effective properties are applied to the fuel regions. The baseline model assumes the DSC is filled with helium gas. Material properties for the effective fuel regions, gases, and solid components are given in the Updated Final Safety Analysis Report (UFSAR [2011]), including surface emissivity values.

2.1.2 Assumptions

The NUHOMS® AHSM-HS with a 32PTH2 DSC is designed for a maximum heat load of 37.2 kW (UFSAR 2011). The heat load was applied to the active fuel length of 150 inches (381 cm) for the CE 16x16 fuel. The active fuel length is positioned 4 inches (10.16 cm) from the inner bottom end of the DSC. The heat load was assumed to be divided into three different heat loading zones and an axial peaking factor was applied along the heated length. Internal radiation was included in the gas regions and surface emissivity values from the UFSAR were applied along the inner surfaces. External convection and radiation were applied along the outer vertical and top horizontal concrete surfaces of the AHSM-HS. The external convection coefficients were calculated based on the natural convection coefficient correlations (Holman 1997) shown in Table 2-1.

Table 2-1. Natural Convection Correlations

Surface	Laminar	Turbulent
Vertical plane or cylinder	h=1.42(ΔT/L)^(1⁄4)	*h*=1.31(Δ*T*)^(1⁄3)
Horizontal plate facing upward	h=1.32(ΔT/L)^(1⁄4)	*h*=1.52(Δ*T*)^(1⁄3)

A k-omega shear stress transport (SST) turbulence flow model (Menter, 1994) was applied to the cooling air region where the flow is driven by natural convection. The k-omega SST model uses the Reynolds-averaged Navier-Stokes (RANS) equations to solve for the fluid flow. The inlets to the air region were set to stagnation inlets and a pressure outlet was applied to each outlet. Laminar flow was assumed in the internal canister gas region. The Boussinesq model was applied to this laminar flow region to provide a buoyancy source term.

For the baseline model a conservative ambient temperature of 100°F (37.8°C) was assumed. This is very close to the hot normal storage ambient temperature of 104°F (40°C) given in the UFSAR (2011). An equivalent soil conduction boundary was applied at the concrete base of the storage assembly and assumed a conservative soil temperature of 68°F (20°C) at a distance three feet below the bottom surface of the AHSM-HS.

Solar loads were applied to all external concrete surfaces of the AHSM-HS exposed to the external environment. The solar loads were based on insolation data presented in the Code of Federal Regulations for Packaging and Transportation of Radioactive Material (10 CFR 71.71) for total heat load over 12 hours. The solar insolation was applied as a solar flux averaged over 24 hours for a steady state analysis. The following insolation values were applied in the STAR-CCM+ model:

- flat horizontal surfaces = 775.32 W/m^2
- curved surfaces = 387.67 W/m^2
- flat non-horizontal surfaces = 193.83 W/m^2

Future work is recommended to look at a more realistic solar loading profile for a marine coastal site than the solar loadings given in 10 CFR 71.71. The current model is for a steady state analysis, and future work will look at the impact of a transient analysis with changing environmental conditions.

2.1.3 Gaps and Contact Resistances

Small gaps that were not explicitly modeled and thermal resistances between contacting parts were modeled with a contact resistance in STAR-CCM+. For parts contacting under a low pressure, a small gap was assumed between parts, and Equation 2.1 was used to calculate the contact resistance.

$$R = \frac{L_{gap}}{k_{gas}} \quad (2.1)$$

where;

R = contact resistance [m^2-K/W]

L_{gap} = gap between parts [m]

k_{gas} = thermal conductivity of gas [W-m/K]

For parts with some amount of metal-to-metal contact (no continuous gap between parts) and assuming there is not a high pressure between the contacting surfaces, a contact resistance was calculated assuming a very small 0.01-inch (0.0254 cm) gap between parts. The gaps assumed for the various part interfaces are shown in Table 2-2. The gaps do not account for thermal expansion between parts. These values generally follow those used in the UFSAR (2011), except for the contact resistance between the canister shell and transition rails, which is much smaller. This is one of the inputs changed when measurements were possible in the canister only tests (see Section 2.3).

Table 2-2. Gaps for STAR-CCM+ Models

Interface Between Parts	Gap Value [in]
Channel Box/Inner Bottom Cover Plate	0.01
Basket/Inner Bottom Cover Plate	1.01
Basket/Channel Box	0.01
Basket/Rails @ 45 deg	0.019
Basket/Rails @ 90 deg	0.023
Canister Shell/Rails	0.1
Fuel/Inner Bottom Cover Plate	1.01

2.1.4 Meshing

The SolidWorks geometry was imported into STAR-CCM+. The geometry was then meshed into regions connected by interface boundaries, resulting in a single conformal polyhedral volume mesh across all regions. Along each wall/fluid interface, the mesh contains prism cell layers to improve the accuracy of the flow solution near the walls. The prism cell layer consists of orthogonal prismatic cells adjacent to the wall boundaries. Figure 2-2 shows the resulting mesh for the baseline model.

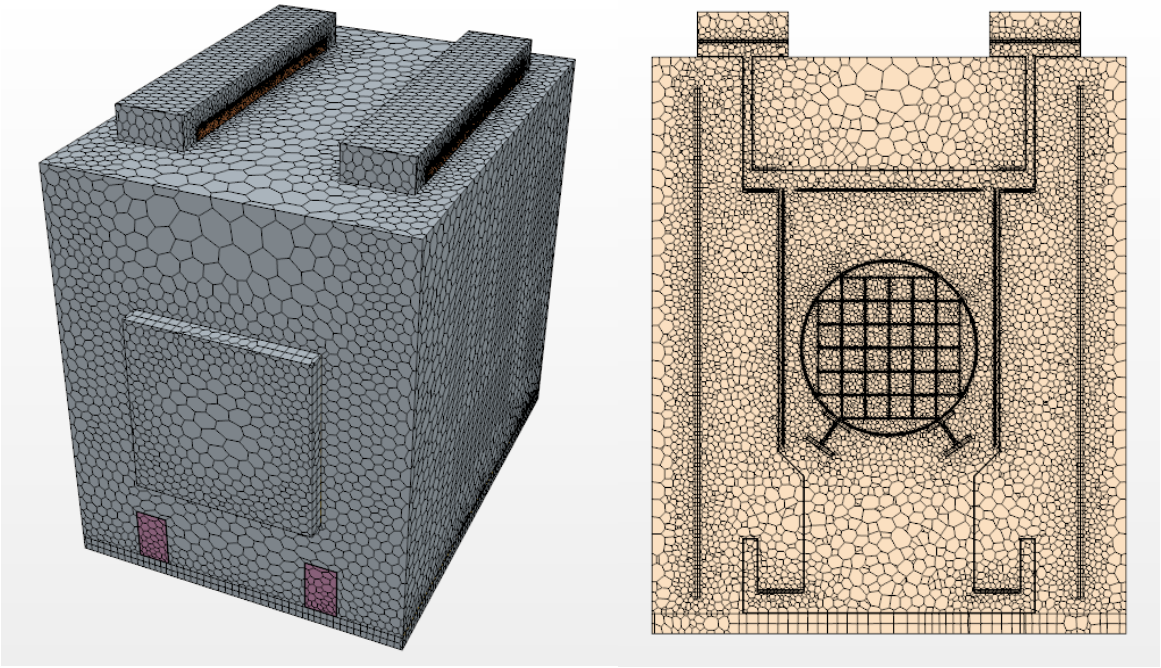

Figure 2-2. Mesh of Baseline AHSM-HS with 32PTH2 Model (a) Overall Mesh and (b) Radial Cross-sectional View of Mesh Through the Center of the AHSM-HS

2.1.4.1 Turbulence and Prism Layer Sensitivity Study

Traditionally, the focus of the Pacific Northwest National Laboratory (PNNL) thermal models has been on the peak cladding temperature for SNF content, but with the focus of CDFD testing to support prediction of stress corrosion cracking (SCC) of the canister, there is a need to take a closer look at the canister surface temperatures. In this case, the canister is represented by the DSC. A sensitivity study was run with the baseline model to look at turbulence model and boundary layer settings. The maximum heat load of 37.2 kW was used for the sensitivity analysis.

Historically, the PNNL SNF storage thermal models have used the k-omega SST turbulence model. The k-epsilon model is another popular turbulence model option in commercial CFD codes. In STAR-CCM+ the default k-epsilon model is the realizable k-epsilon model (Shih, 1995). The k-omega models tend to give better predictions for boundary layer flow near surfaces than the k-epsilon models (Andersson et al., 2012). Cases for the sensitivity analysis were run with both the k-omega SST and realizable k-epsilon. For all cases, the average wall Y+ value, which is a dimensionless measure of near-wall cell spacing, was kept ≤ 1. This was controlled by the thickness and number of cells within the boundary layer, represented by the orthogonal prismatic cells in STAR-CCM+. The total thickness of the prism layer cells, was varied between runs (the number of prism layers was selected to keep the wall Y+ values below 1). Results are shown for the canister average and maximum temperature in Figure 2-3 and Figure 2-4. For both the average and maximum canister temperature, the k-omega SST model resolved to a stable temperature as the total prism layer thickness increased, while the realizable k-epsilon model did not vary significantly as the prism layer thickness changed. At a prism layer thickness of 1 cm the average and maximum canister temperature predicted by the k-omega and k-epsilon models differs by 4˚C and 7˚C respectively. As the prism layer thickness increases, the predicted temperature differences between the k-omega and k-epsilon cases decreases and at a prism layer thickness of 4 cm both the average and maximum canister temperatures predicted by the k-omega and k-epsilon models are within 2˚C of each

other. The k-omega SST turbulence model with 20 prism layers having a total thickness of 4 cm was used in the thermal and deposition models.

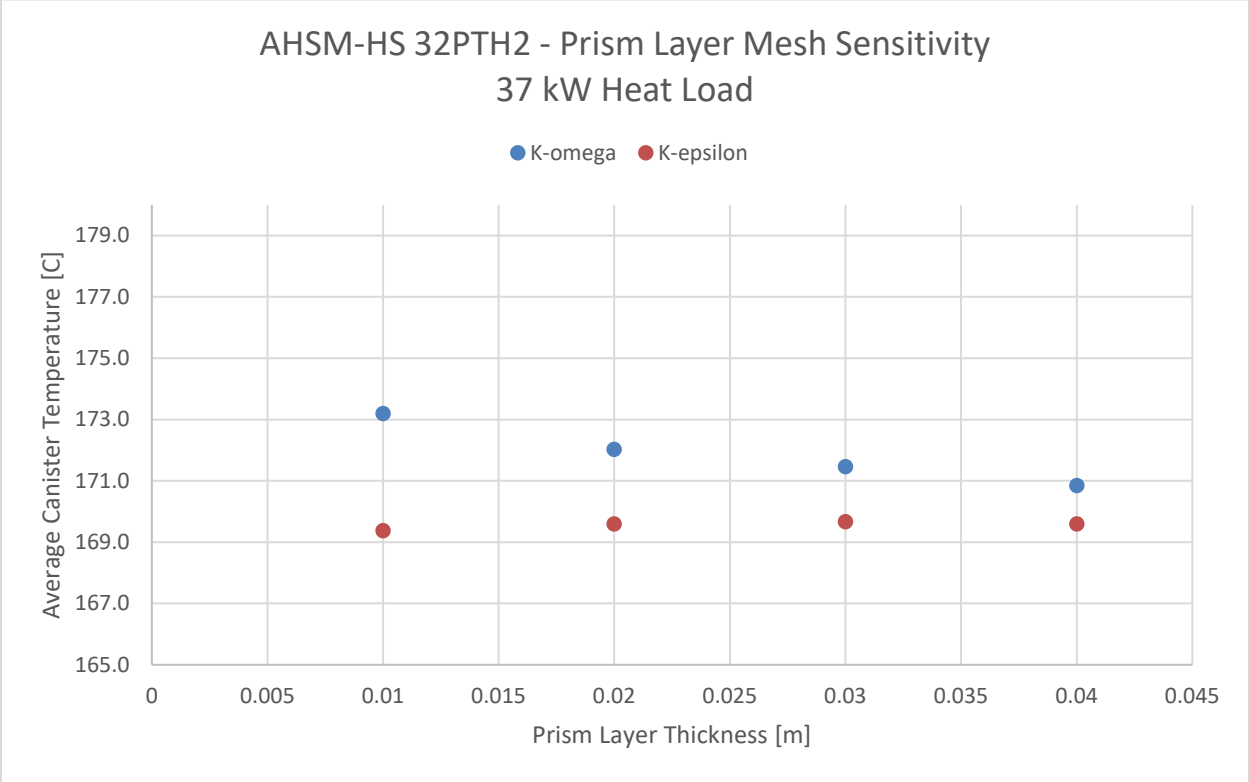

Figure 2-3. Average Canister Temperature with 37.2 kW Heat Loading

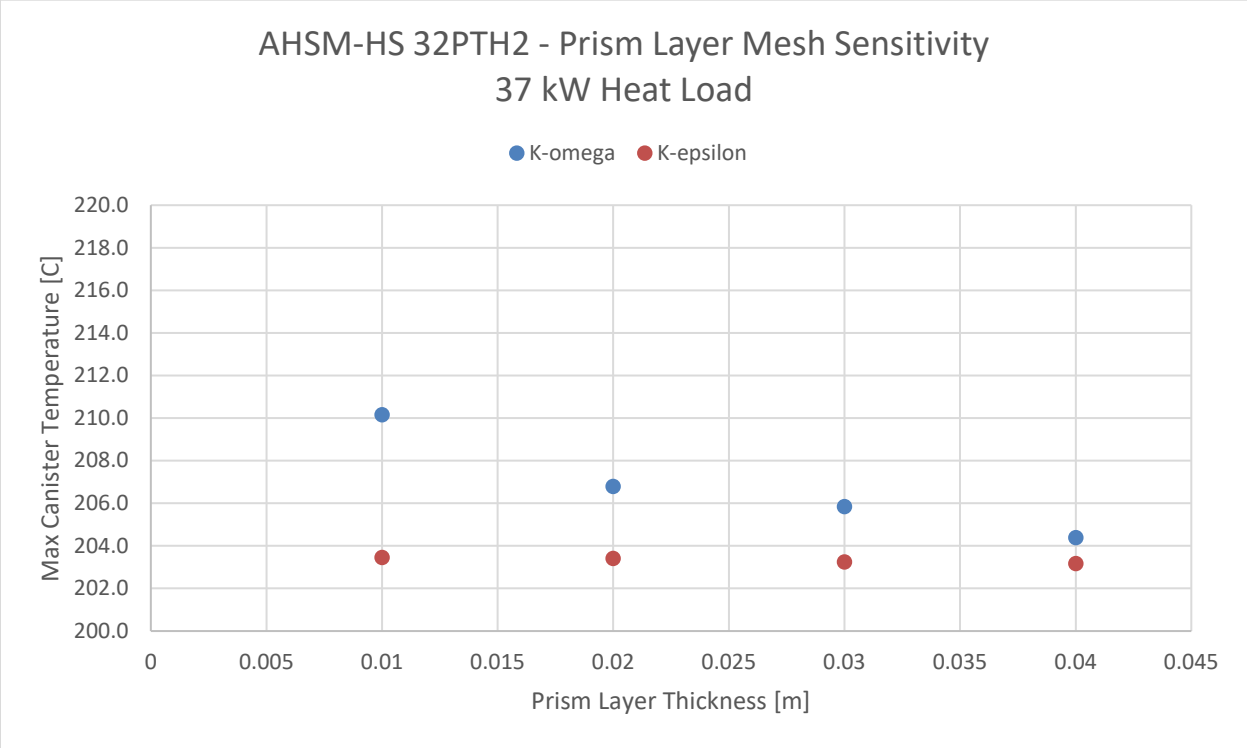

Figure 2-4. Maximum Canister Temperature with 37.2 kW Heat Loading

2.1.5 Single AHSM-HS Model

The baseline model representing a single AHSM-HS module was run at the maximum designed heat load of 37.2 kW. The resulting temperature contour plots are shown in Figure 2-5. The baseline model gives a peak cladding temperature (PCT) of 387°C. The non-proprietary UFSAR gives a PCT of 386°C for this case (UFSAR 2011). It should be noted that the baseline model assumed an ambient temperature of 100°F (37.8°C) while the UFSAR model was run with an ambient temperature of 104°F (40°C). An additional difference is in the treatment of the basket (see Section 2.3.4), but consistent results at this point suggested the model was working well and ready for use in developing the models described below and for comparison with the electrically heated canister (Section 2.2.2).

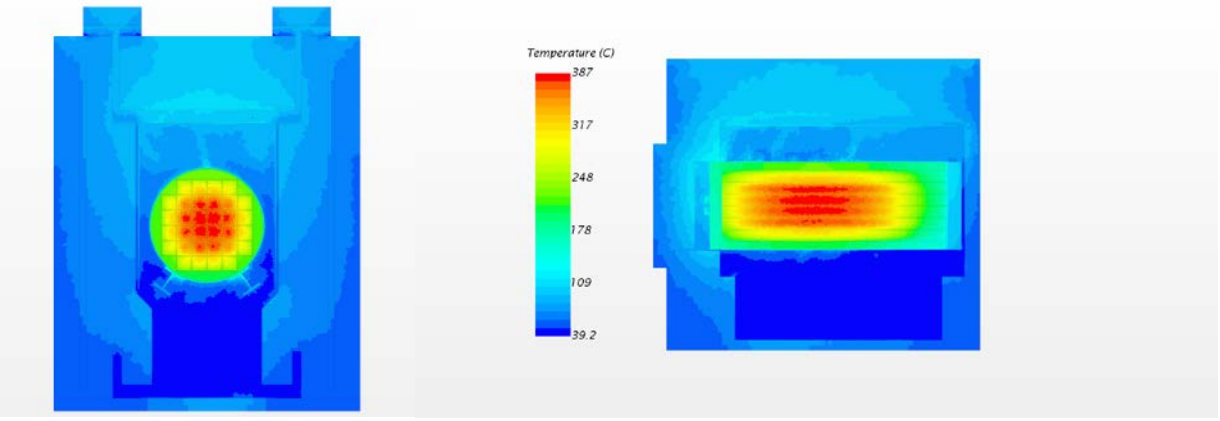

Figure 2-5. Radial and Axial Temperature Contour Plot Through the Center of the Baseline AHSM-HS 32PTH2 Model

2.1.6 Three AHSM-HS Model

The current plan for the CDFD project is to have three modules assembled in a row, with each module having a unique heat load. There will be a "high heat" canister with a heat load of 40 kW, a "low heat" canister with a heat load of 10 kW, and a "no heat" canister that is unheated. The NUHOMS® AHSMs' are designed to be attached to an adjacent module with shared inlets. This creates a challenge for isolating modules from each other, especially for the no heat canister. An intermediate wall is currently being designed to be placed between modules to help isolate the heated canisters from the no heat canister.

2.1.6.1 Insulated Intermediate Wall

The intermediate wall will separate the shared inlets between adjacent modules and enclose the end modules. Within each wall will be an embedded layer of polyiso[a] insulation. The three modules with intermediate walls are shown in Figure 2-6.

[a] See, for example, https://www.dyplastproducts.com/data-sheets-isoht

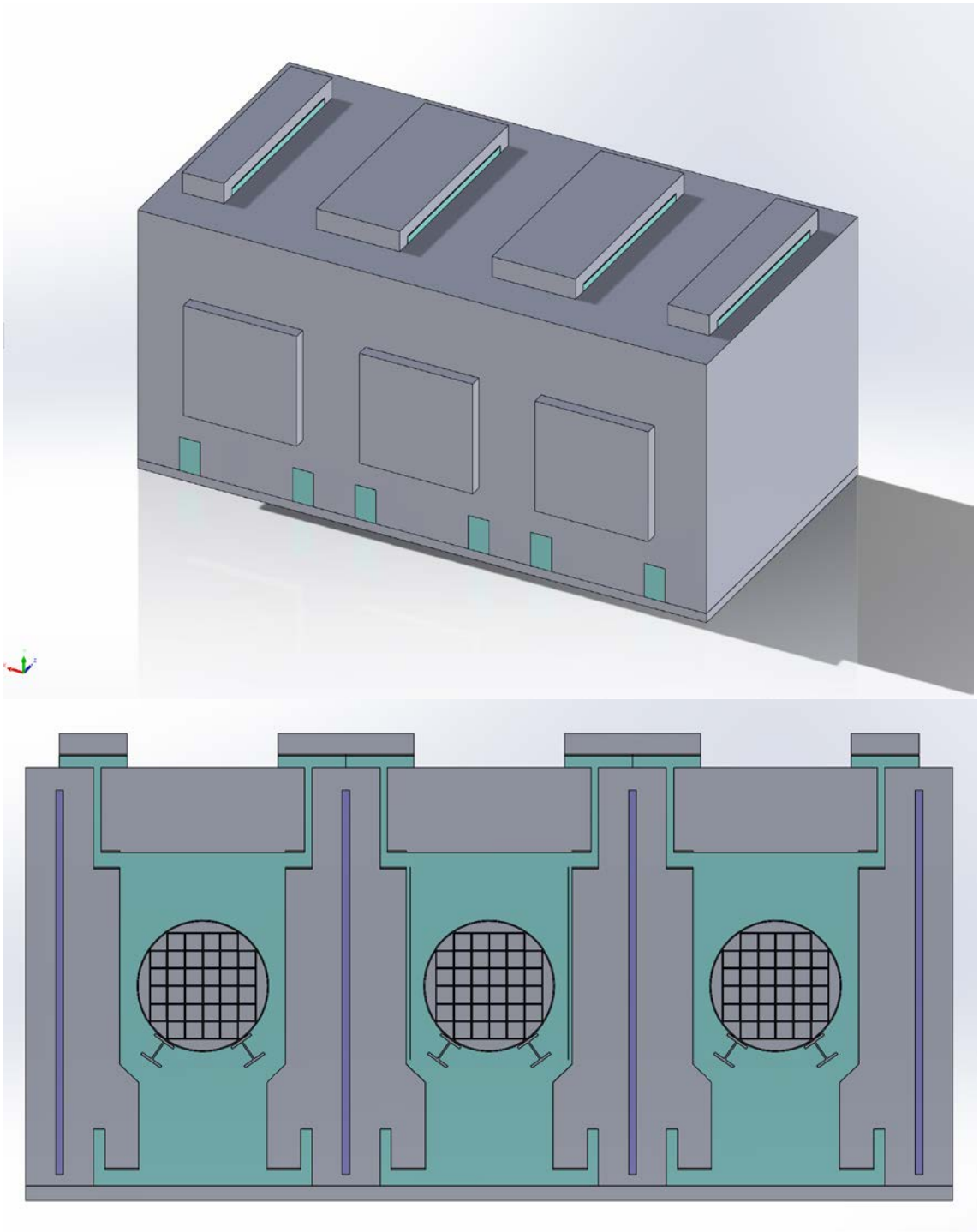

Figure 2-6. Three AHSM-HS Model Geometry with Intermediate Walls (a) External View and (b) Cross-Sectional View through the Center of the AHSM-HS

The plan is to have the no heat canister in the center with the high and low heat load canisters on the ends. The thermal model was used to look at both the effectiveness of adding insulation to the intermediate wall and how thick the insulation needs to be. A sensitivity study was run to look at the high heat canister adjacent to the no heat canister and joined by an intermediate wall. The two adjoining modules were modeled as half-symmetry models (the modeled half of the high heat canister had a total heat load of 20

kW). The thickness of the polyiso insulation within the intermediate wall was varied between runs. The results of the sensitivity study are shown in Figure 2-7, which plots the heat transferred along the shared boundary between the modules versus insulation thickness. The plot also shows the heat transferred to the cold module with no intermediate wall separating the AHSMs. For this case approximately 43% of the total heat load from the high heat module is transferred to the no heat module. The thermal model showed that 4-inch (10.16 cm) thick polyiso insulation was sufficient for isolating the heat transfer between modules. This reduced the heat transferred from the high heat module to the no heat module down to approximately 1%.

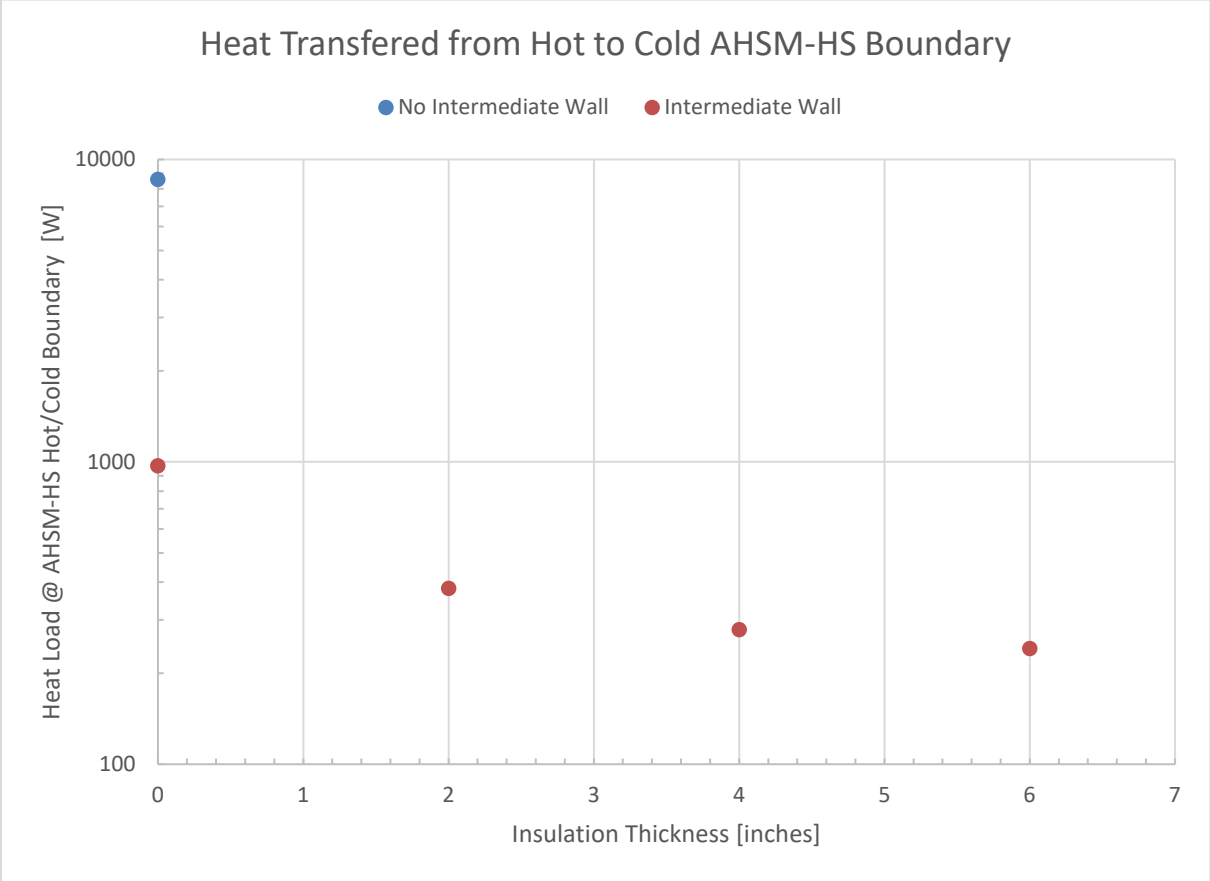

Figure 2-7. Heat Transferred from the High Heat Load Module to the No Heat Module Along the Shared Intermediate Wall Versus Insulation Thickness

The three AHSM-HS model was run with CE 16x16 fuel represented with solid homogeneous regions (as described in the baseline model). The model was run with an average temperature more representative of a marine coastal site. A yearly average temperature of 75.7°F (16.1°C) was selected. The resulting temperature contour plots of the three DSCs are shown in Figure 2-8. The temperature plot shows that the intermediate wall, with 4 inches (10.16 cm) of polyiso insulation, is predicted to sufficiently insulate the no heat canister from the neighboring heated canisters. Natural convection flow in the no heat canister will be primarily driven by solar loads.

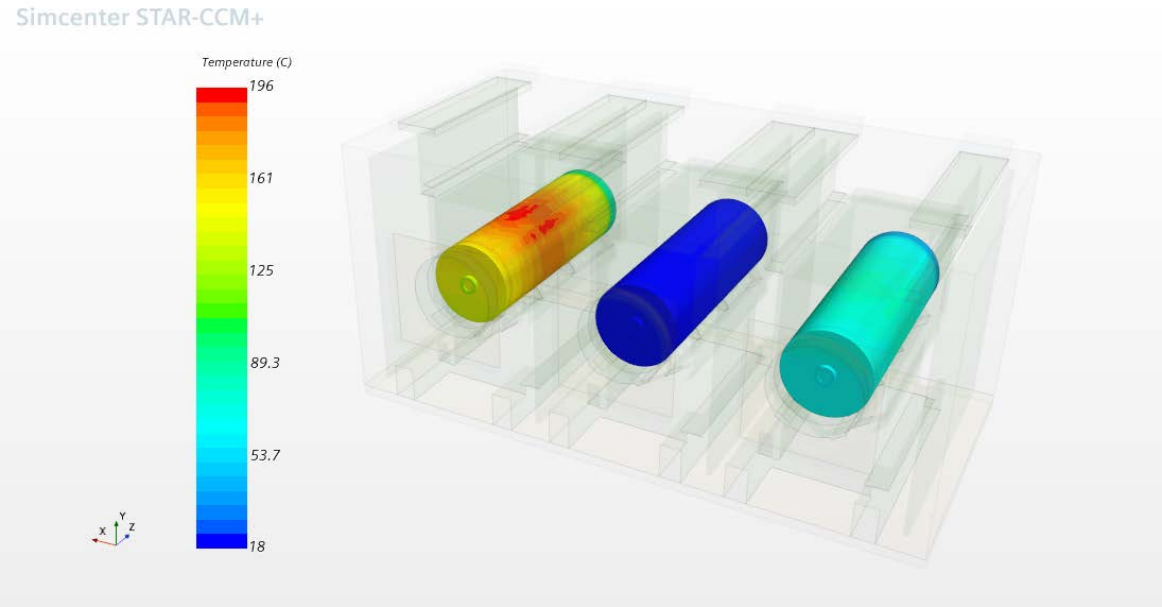

Figure 2-8. Three AHSM-HS Thermal Model – DSC Temperature Contour Plot

2.1.7 Wind Effects Model

An external fluid region was added to the single and three AHSM-HS modules to create wind effects models. This external fluid region was built based on recommended best practices for external aerodynamics [Siemens 2020a, Siemens vehicle 2020b]. The wind effects for various wind speeds needs to be studied, because some sites may have highly variable wind patterns.

2.1.7.1 Wind Effects Three AHSM-HS Model

The domain fit to the three-AHSM-HS model is a half sphere with a radius of 125 meters. This is approximately ten times the width of the three-module system. This domain size removes any effect of the outer boundary conditions (Siemens 2020a). The semi-sphere shape of the domain was based on best practices for aerospace vehicles (Siemens 2020b). The half sphere geometry allows for analyzing a variety of different external flow directions without having to change external boundary conditions. The domain size is based on road-going vehicles rather than aerospace vehicles because the flow conditions for this application are closer to road vehicles. Aerospace vehicles experience air speeds greater than Mach 0.3, which requires different physics continua and the large boundaries recommended in (Siemens 2020b).

To ensure the model with the external fluid region is similar to the starting standalone three AHSM-HS model (described in Section 2.1.6), the external fluid model was run under stagnant conditions. The outer boundary of the external fluid region was set as a pressure outlet boundary. When using this boundary while including the effects of gravity in STAR-CCM+, an external boundary pressure correction is applied to prevent nonphysical recirculation at the boundary. The following equation is applied to the boundary,

$$P_{correct} = P_{ref}\left(e^{\frac{-gz}{R+T_{amb}}} - 1\right) + g\rho_{ref}z$$

Where,

$$\rho_{ref} = \frac{P_{ref}}{RT_{amb}}$$

$$g = 9.81 \text{m/s}^2$$

$$P_{ref} = \text{ambient pressure } (pa)$$

$$T_{amb} = \text{ambient temperature } (K)$$

$$R = 287.058\, J/kg - K$$

$$z = \text{elevation } (m)$$

The three AHSM-HS wind effects models were run as a natural convection case (no wind) to compare with the standalone thermal model. Figure 2-9 shows a radial cross-section temperature contour plot through the center of the AHSMs for both the standalone and wind effects model. The wind effects and standalone models compare well with each other, with the PCT within 1˚C. Table 2.3 shows the maximum temperatures for a few components in the AHSM-HS. All of them compare very well except for the concrete external temperatures, which are about 18°C different. This difference is due to the influence of solar radiation on the outside surfaces of the AHSM-HS. These two models have different implementations of solar radiation due to the treatment of the external environment. The solar radiation and external temperature of the concrete has little effect on the peak temperature of the fuel inside the AHSMs because most of the heat transfer occurs via natural convection through the vents in the system. The total air mass flow rate through the system is slightly different between the two models. This is again due to the difference in environment around the inlets and outlets of the AHSM-HS canister. Despite this small difference in air mass flow, the maximum fuel and canister temperatures are nearly identical.

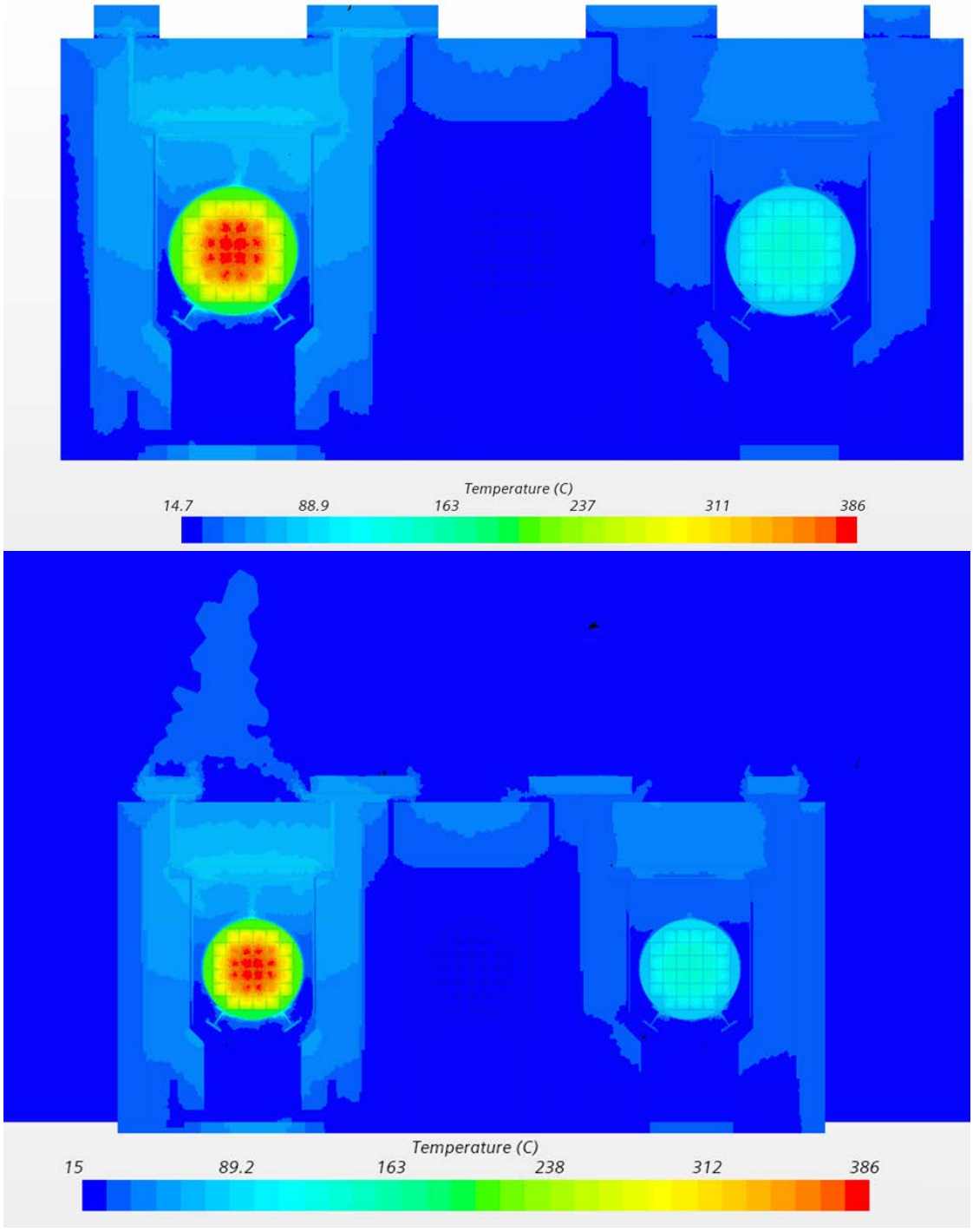

Figure 2-9. Radial Cross-Section Temperature Contour Plots of Natural Convection Cases for Three AHSM-HS (a) Standalone Model and (b) Wind Effects Model

Table 2-3. Maximum Temperature Comparisions and Mass Flow Rate Between the Stand Alone and Wind Effects STAR-CCM+ Models

Model	Max Temp Fuel [°C]	Max Temp Canister [°C]	Max Temp Concrete Ext Surface [°C]	Total Mass Flow [kg/s]
Stand Alone 3-Module	389	195	79	1.57
Wind Effects	388	196	61	1.65

2.1.7.2 Wind Effects Single AHSM-HS Model

The single standalone AHSM-HS thermal model from Section 2.1.5 is used as the basis for wind effects modeling. To be configured for wind effects, this model is setup with a 55-meter radius semi sphere to model external fluid (wind) flowing over the cask shown in Figure 2-10. This was loosely based on best practices for vehicle external aerodynamics on an open road (Siemens 2020a). The flow domain comes out to about 9 times the length of the casks analyzed. Using a halfsphere rather than a square box domain allows for rotating the flow around the cask without having to change the boundary types on the desired inflow and outflow boundaries. This semi sphere boundary enables these cask system models to be used for a variety of studies, which is helpful for wind effects and particle deposition studies. This single AHSM-HS wind effects model was used to run sensitivities to wind direction.

Figure 2-10. Single AHSM-HS with External Fluid Boundary Applied

A previous study with a different NUHOMS® geometry found backflow through one of the outlets at certain wind directions (Jensen et al., 2020b). For this current study a wind sweep was performed on a single module AHSM-HS to determine if this backflow condition exits for this AHSM-HS cask. For these cask systems, the external flow is dependent on the geometry of the cask. This wind sweep was performed by changing the wind direction in 30° increments with 0° being normal to the inlets of the cask. Also, 45° and 135° wind directions were tested in addition. All wind directions were run with a 5

m/s wind speed. These test conditions are similar to the previous wind effects study in (Jensen et al., 2020b).

The mass flow results of this wind sweep for the single AHSM-HS are shown in Table 2-4. Positive mass flow is into the cask and negative is out. For all wind directions there is little evidence of backflow through the outlets of the cask as all mass flow rates are negative. For the 135° wind direction, back quartering direction, the mass flow through the left outlet was relatively low, which indicates a higher likelihood of backflow occurring through that outlet, but the mass flow out of that outlet is still negative, which indicates outflow and no backflow. The locations of the inlets and outlets are depicted in Figure 2-11. For a 5 m/s wind speed at 135° there is no backflow, but further investigation is necessary to determine that this holds for all windspeeds. The AHSM-HS outlets are open on two sides, allowing wind-blown air to pass from one side of the outlet to the other, instead of taking a 90° turn into the AHSM-HS module. Outlet geometry is an important factor in the development of backflow. It is also important to note that it has not been determined if backflow has any adverse impacts. Some designs may be more susceptible to backflow than others and further investigation of backflow conditions and its impact is recommended.

Along with the mass flow sensitivities, the thermal responses from changing wind directions is shown in Table 2-5. The environmental conditions for this run are 38°C (100°F) ambient temperature and a 40kW heat load. The hottest canister and fuel temperature occurred at the 90° wind direction. At that wind direction, the wind is blowing across the inlets, impeding airflow into the cask. The maximum fuel temperature for this case was 2°C warmer than the stagnant case. As the wind rotated toward the back of the module the temperatures decreased but were still warmer than when the wind direction was normal to the inlets of the cask. Wind flow normal to the inlets significantly increased the air flow rate through the cask thus lowering canister and fuel temperatures.

Table 2-4. Mass Flow Into (+) and Out of (-) the Cask.

Wind Direction[1] [deg.]	Mass Flow Inlet Left [kg/s]	Mass Flow Inlet Right [kg/s]	Mass Flow left Outlet [kg/s]	Mass Flow Right Outlet [kg/s]
0	0.75	0.75	-0.75	-0.75
30	0.70	0.68	-0.57	-0.81
45	0.62	0.62	-0.40	-0.84
60	0.60	0.51	-0.32	-0.79
90	0.33	0.33	-0.37	-0.33
120	0.36	0.42	-0.21	-0.56
135	0.38	0.42	-0.17	-0.60
150	0.35	0.43	-0.38	-0.36
180	0.44	0.44	-0.44	-0.43

1. 0° wind direction corresponds to the wind being normal to the inlets of the cask.

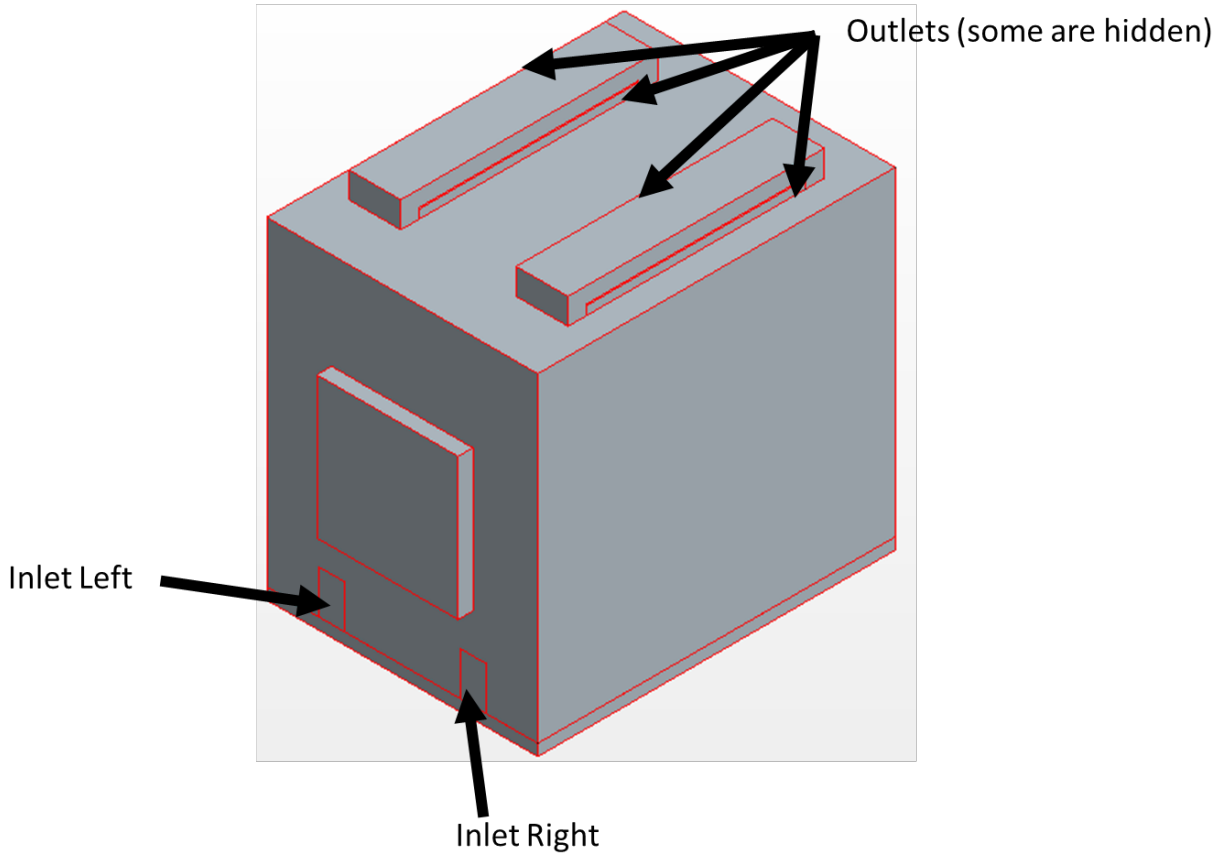

Figure 2-11. Diagram of the Inlets and Outlets on the AHSM-HS Single Module

Table 2-5. Thermal Response to Changing Wind Directions

Wind Direction [deg.]	Max. Temp. Fuel [°C]	Max. Temp. Canister [°C]	Average Temp. Fuel [°C]	Average Temp. Canister [°C]
0	394	205	274	166
30	396	206	275	168
45	397	207	277	170
60	399	210	280	172
90	408	218	289	180
120	405	215	286	178
135	406	216	287	179
150	406	215	287	179
180	403	214	283	175

2.2 Heater Assembly Models

For the CDFD project the SNF assemblies within the 32PTH2 DSC will be replaced with electrical heater assemblies. The heater assemblies are being designed by Sandia National Laboratories (SNL).

2.2.1 Heater Assembly Description

The thermal model was used to aid SNL in the evaluation of various heater designs. A goalpost radiative style heater was chosen for the CDFD project and is described in Lindgren et al. (2021). The heater assemblies have a U-tube heater connected to a stainless-steel C-channel backbone with stainless-steel goalposts. At each end of the heater assembly are thermal radiation shields. The thermal model indicates that these shields are necessary to replicate a more prototypic canister surface temperature distribution. The baseline model was modified with the heater assemblies. The CAD geometry of the heater assemblies is shown in Figure 2-12.

Figure 2-12. CAD Geometry for Electrical Heater Assemblies

In addition to replacing the SNF assemblies with the goalpost heater assemblies, the following modifications were also made to the heater assembly model to replicate test conditions:

- The fill gas within the canister was changed to air (it is helium in the baseline model).
- Parts of the lid were removed. This included removing the outer cover and top shield plug. The inner cover was moved to sit against the support ring.

2.2.2 Comparisons with Baseline Model

Canister surface temperature comparisons of the goalpost heater model and the baseline SNF model are shown in Figure 2-13. Overall, the heater assembly model compares well with the baseline SNF model.

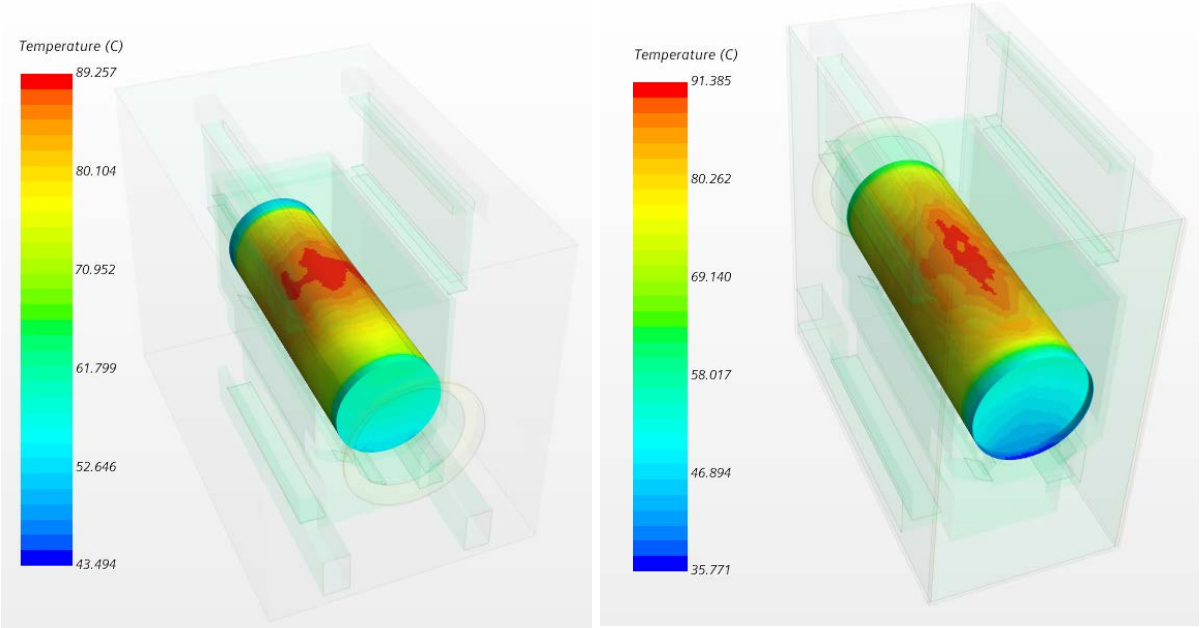

Figure 2-13. DSC Temperature Contour Plots of (a) Baseline Model and (b) Heater Assembly Model

2.3 Canister Model with Prototypic Heaters

SNL conducted a preliminary heater test within a 32PTH2 canister to verify the proposed heater design (Lindgren et al., 2021). The testing consisted of a 32PTH2 DSC, with no AHSM-HS overpack, sitting on insulated blocks in an open room. A STAR-CCM+ model which was constructed to simulate the preliminary heater testing and the geometry is shown in Figure 2-14.

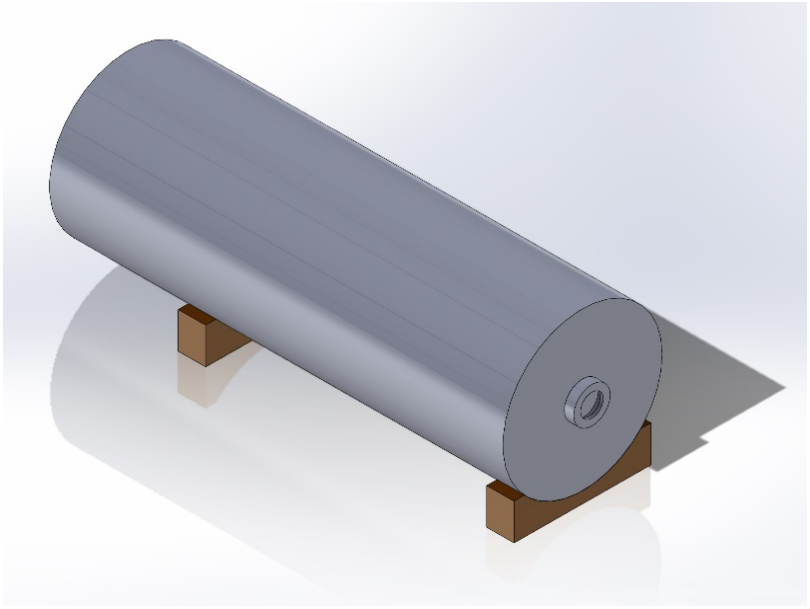

Figure 2-14. CAD Geometry of Canister Model with Prototypic Heaters

2.3.1 Experimental Setup

A total heat load of 9.60 kW was applied uniformly to eight prototypic heater assemblies. Four of the heater assemblies are located within the center most basket positions and four near the corners of the basket. It took approximately four days for the canister to reach steady state temperatures. Thermocouples were placed along the outer surface of the canister and against internal components, such as the heater rods. Details of the preliminary testing are given in Lindgren et al. (2021).

2.3.2 Model Description

A cross-sectional plot of the CAD geometry for the canister model with prototypic heaters is shown in Figure 2-15. The position of the eight prototypic heater assemblies within the DSC and the coordinate system for the thermocouples along the external DSC surface can be seen in Figure 2-15. The zero-degree thermocouple corresponded to the top of the canister, the 180 degree position to the bottom of the canister, and the sides of the canister were represented by the 90 degree and 270 degree locations.

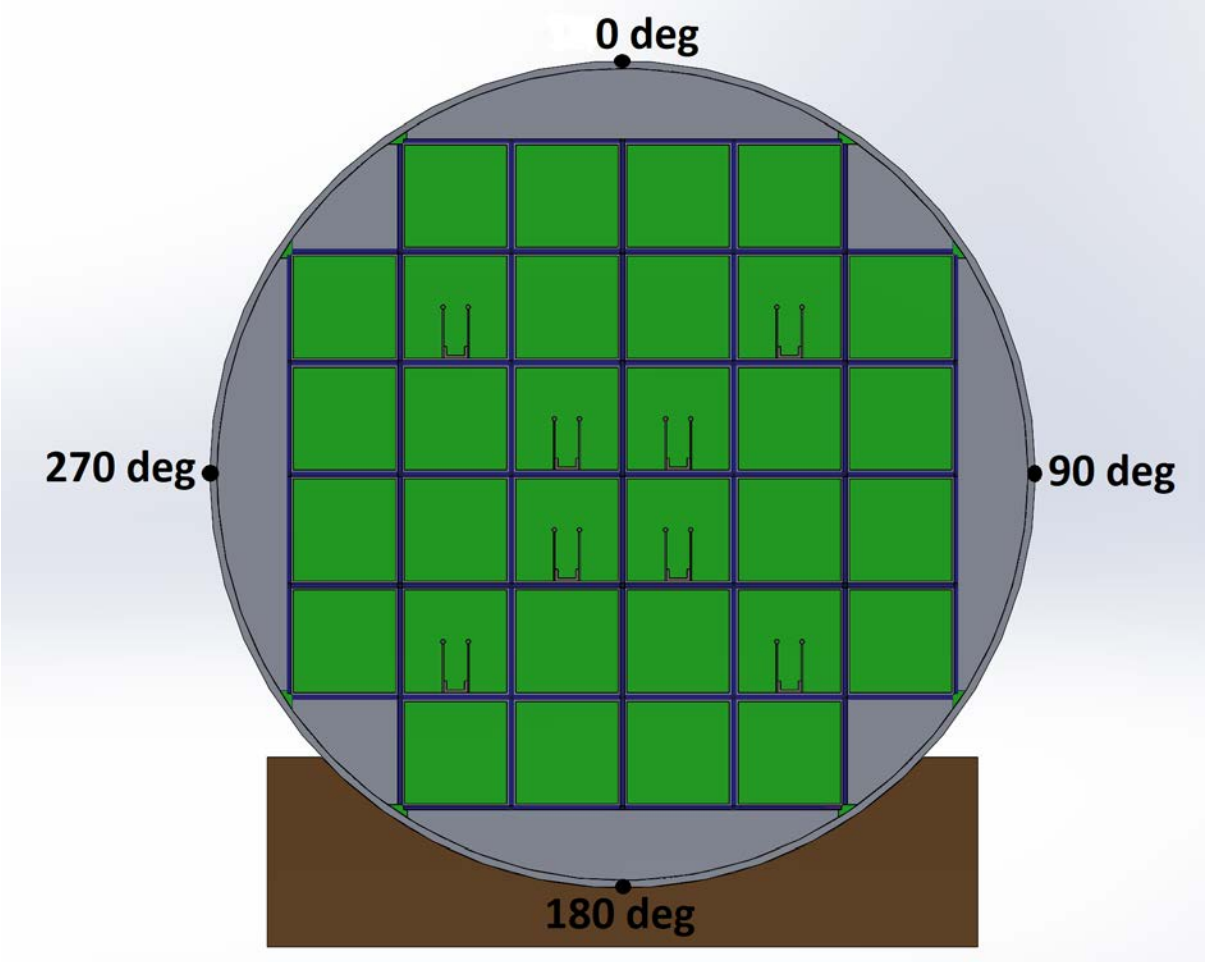

Figure 2-15. Cross-sectional Plot of CAD Geometry For Canister Model with Prototypic Heaters. Thermocouple Cylindrical Positions Shown along the External Surface of the DSC

SNL took measurements of the gap between the basket rails and the canister shell. These measurements were taken both at an ambient condition and at the 9.6 kW heat load. The resulting measurements are shown in Table 2-6. The gap varies with angular position. It should be noted that these measurements are preliminary.

Table 2-6. Preliminary Measurements for the Gap between the Canister Shell and Basket Rails

Gap Measurements (in.)		
Degrees	**Ambient**	**9600 W**
0	0.30	0.30
30	0.27	–
60	0.28	0.25
77	0.31	0.23
103	0.23	0.20
120	0.06	–
180	0.00	0.00
240	0.14	–
250	0.16	0.03
270	0.20	0.13
300	0.19	0.20
330	0.23	0.25

The data points shown in Table 2-6 for the 9600 W measurements were input into STAR-CCM+ as a table and the gap value was calculated based on angular position and interpolating between table values. The resulting gap was used to calculate a variable contact resistance between the canister shell and basket rails based on angular position. This gap was the only source of asymmetry in the STAR-CCM+ model.

2.3.3 Initial Comparisons with Measured Thermocouple Data

The steady state results for the STAR-CCM+ canister model with prototypic heaters are shown in Table 2-7. Measurement results are taken from Lindgren et al. (2021). Canister temperatures are shown for the thermocouples located axially along the canister at 85.375 inches (216.85 cm) from the external bottom surface of the canister. This axial distance corresponds to the center of the heated zone. The peak heater temperature (PHT) is taken as the maximum temperature of the thermocouple heater rods. The steady state measurement was taken at approximately 120 hours.

Table 2-7. Initial Steady State Model Results and Comparison with Measured Thermocouple Data

Thermocouple	Temperature [C]	
	Measurement	STAR-CCM+
PHT	417	384
TC - Canister 0 deg @ 85.375 in	61	58
TC - Canister 90 deg @ 85.375 in	73	61
TC - Canister 180 deg @ 85.375 in	81	79
TC - Canister 270 deg @ 85.375 in	74	66

The results in Table 2-7 show that the STAR-CCM+ model significantly underestimates the PHT. The model also underpredicts the side temperatures along the external canister surface. These differences between the measured and predicted model data are believed in part to be due to simplifications made in the modeling of the basket. The initial STAR-CCM+ model represents the fuel compartments explicitly, but it uses a simplified treatment of the poison plates and connecting plates between the fuel compartments. It was assumed that the poison plate and connecting plate assembly could be represented as a single region with isotropic properties. Since this assembly is composed of stainless steel, aluminum, and poison plates along with associated gaps, a more accurate representation would have orthotropic properties.

2.3.4 Model Refinements

A more representative basket geometry was constructed, and orthotropic properties calculated. The basket CAD geometry was updated to split the basket into three separate regions; a vertical section, horizontal section, and overlapping region that represents the intersection between the horizontal and vertical sections. Figure 2-16 shows a cross-section of the CAD geometry of the updated detailed basket geometry with the three separate regions.

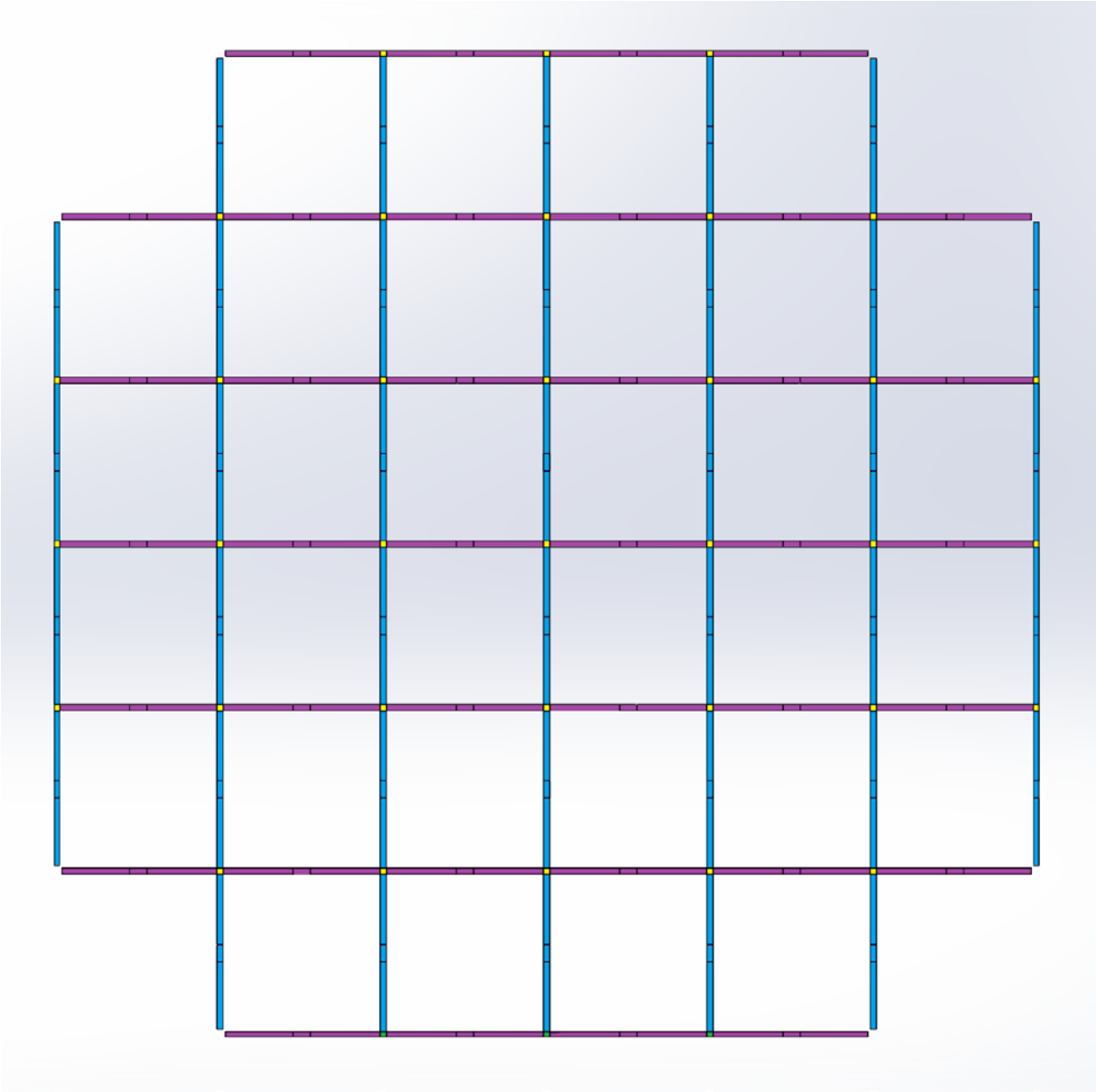

Figure 2-16. Detailed Basket Geometry Showing the Three Separate Basket Regions (Shown in Blue, Purple, and Yellow)

The effective thermal conductivities of the basket components were calculated based on the direction of heat transfer through or along the basket wall. The basket walls have a complex geometry with layered sections of aluminum and poison plates, stainless-steel components, and gas gaps of various sizes throughout. This means that the rate of heat transfer through the basket walls would be different depending upon the direction of heat transfer. The exact configuration of the basket walls is proprietary, as are some of the thermal properties of the specialized materials. Although these values cannot be shared in this report, they were used in the effective conductivity calculations. For a given dimension (along the axial length or through the basket wall, for example), the different parallel heat conduction paths were identified. For each of these paths, a serial thermal resistance was calculated. Next, the overall effective thermal conductivity was calculated by adding the path resistances in parallel. This principle was applied in all three dimensions to generate orthotropic effective thermal conductivities for the basket walls.

The detailed basket geometry was integrated into the canister model with prototypic heaters and the effective properties applied to the three regions. The vertical and horizontal basket regions were given orthotropic thermal conductivity properties. The intersecting section (shown in yellow in Figure 2-17) was given isotropic properties with a magnitude that approximates that of the overlapping plates.

SNL also provided emissivity measurements for the CDFD components. Table 2-8 shows the measured emissivity data. These measurements are preliminary.

Table 2-8. Preliminary Emissivity Measurements for CDFD Hardware

Hardware Component	Measured Emissivity
Shell	0.24
Bottom lid	0.14
Basket	0.31
Out-facing thermal shield	0.16
In-facing thermal shield	0.12
C-channel	0.21
Heater Rod	0.69

The STAR-CCM+ model was updated with the detailed basket and measured emissivity data shown in Table 2-8. Updated results are shown in Table 2-9. Overall, the model compares much better with the measured thermocouple (TC) data after the updates. The model does overpredict the canister temperature along the underside of the canister (180 degrees) and does not show the same asymmetries that the experiment does. This is most likely due to the simplified assumptions made for the heat transfer at the outer canister surfaces. The detailed basket and measured emissivity data will be integrated into the AHSM-HS 32PTH2 model in future work.

Table 2-9. Updated Steady State Model Results and Comparison with Measured Thermocouple Data

Thermocouple	Temperature [C]	
	Measurement	STAR-CCM+
PHT	417	405
TC - Canister 0 deg @ 85.375 in	61	66
TC - Canister 90 deg @ 85.375 in	73	69
TC - Canister 180 deg @ 85.375 in	81	93
TC - Canister 270 deg @ 85.375 in	74	76

2.3.5 Transient Analysis

A transient analysis was run with the updated canister model with prototypic heaters (the updated model includes the detailed basket and updated emissivity values). The steady state model included internal convection within the canister, but for the transient model internal convection was turned off to significantly speed up the transient analysis. To account for convection, an effective thermal conductivity

of air flowing within the DSC was calculated based on the average Nusselt Number (Nu) predicted for the internal air flow in the steady state model. The Nu is a ratio of convective heat transfer to conductive heat transfer. The effective thermal conductivity was calculated by multiplying the thermal conductivity of air by Nu. This approach was tested with the steady state model before running the transient analysis and results comparing the steady state analyses is shown in Table 2-10. Overall, the no convection steady state model results compare reasonably well with the steady state model with convection, especially for the canister surface temperatures. The heater rod temperatures are under predicted in the no convection case, especially for the thermocouples further away from the center of the heater zone (the center of the heated zone is located at 85.375 inches).

Table 2-10. Comparison of Steady State STAR-CCM+ Models Both With and Without Internal Convection Air Flow

Thermocouple	Temperature [C]	
	Steady State STAR-CCM+ Model with No Convection	Steady State STAR-CCM+ Model with Convection
TC - Canister 0 deg @ 40 in	62.2	62.9
TC - Canister 0 deg @ 85.375 in	65.5	66.0
TC - Canister 0 deg @ 128.625 in	63.3	65.2
TC - Canister 90 deg @ 40 in	65.9	66.2
TC - Canister 90 deg @ 85.375 in	69.4	69.2
TC - Canister 90 deg @ 128.625 in	66.8	68.1
TC - Canister 180 deg @ 40 in	88.5	87.8
TC - Canister 180 deg @ 85.375 in	94.9	92.7
TC - Canister 180 deg @ 128.625 in	90.9	91.3
TC - Canister 270 deg @ 40 in	72.6	72.8
TC - Canister 270 deg @ 85.375 in	76.4	76.0
TC - Canister 270 deg @ 128.625 in	73.1	74.6
TC Cell HE- Heater Rod @ 40 in	376.7	391.3
TC Cell HE - Heater Rod @ 85.375 in	400.4	400.2
TC Cell HE - Heater Rod @ 128.625 in	372.6	385.1
TC Cell HF - Heater Rod @ 40 in	376.7	394.1
TC Cell HF - Heater Rod @ 85.375 in	401.9	402.5
TC Cell HF - Heater Rod @ 128.625 in	372.5	386.5
TC Cell HB - Heater Rod @ 85.375 in	391.0	394.8
TC Cell HC - Heater Rod @ 85.375 in	393.0	397.8
TC Cell HA - Heater Rod @ 85.375 in	404.1	405.1
TC Cell HD - Heater Rod @ 85.375 in	401.9	404.6
TC Cell HG - Heater Rod @ 85.375 in	390.9	395.5
TC Cell HH - Heater Rod @ 85.375 in	392.1	395.3
Overall Cell HB Heater Rod Max Temp	399.6	400.6
Overall Cell HC Heater Rod Max Temp	402.1	403.4
Overall Cell HA Heater Rod Max Temp	410.7	410.2
Overall Cell HD Heater Rod Max Temp	410.1	410.1
Overall Cell HE Heater Rod Max Temp	408.4	407.4
Overall Cell HF Heater Rod Max Temp	409.5	408.8
Overall Cell HG Heater Rod Max Temp	399.4	399.8
Overall Cell HH Heater Rod Max Temp	399.4	400.7

The transient analysis incorporated ambient versus time and power versus time data provided by SNL as boundary conditions. The analysis was run out to 124 hours. Figure 2-17 plots the resulting temperatures of the STAR-CCM+ transient analysis compared to the measured data (Lindgren et al., 2021) for the thermocouples located at the center of the axial heated zone (85.375 inches). Apart from the TC located on the underside of the canister at 180 degrees, the model results compare reasonably well with the measured data.

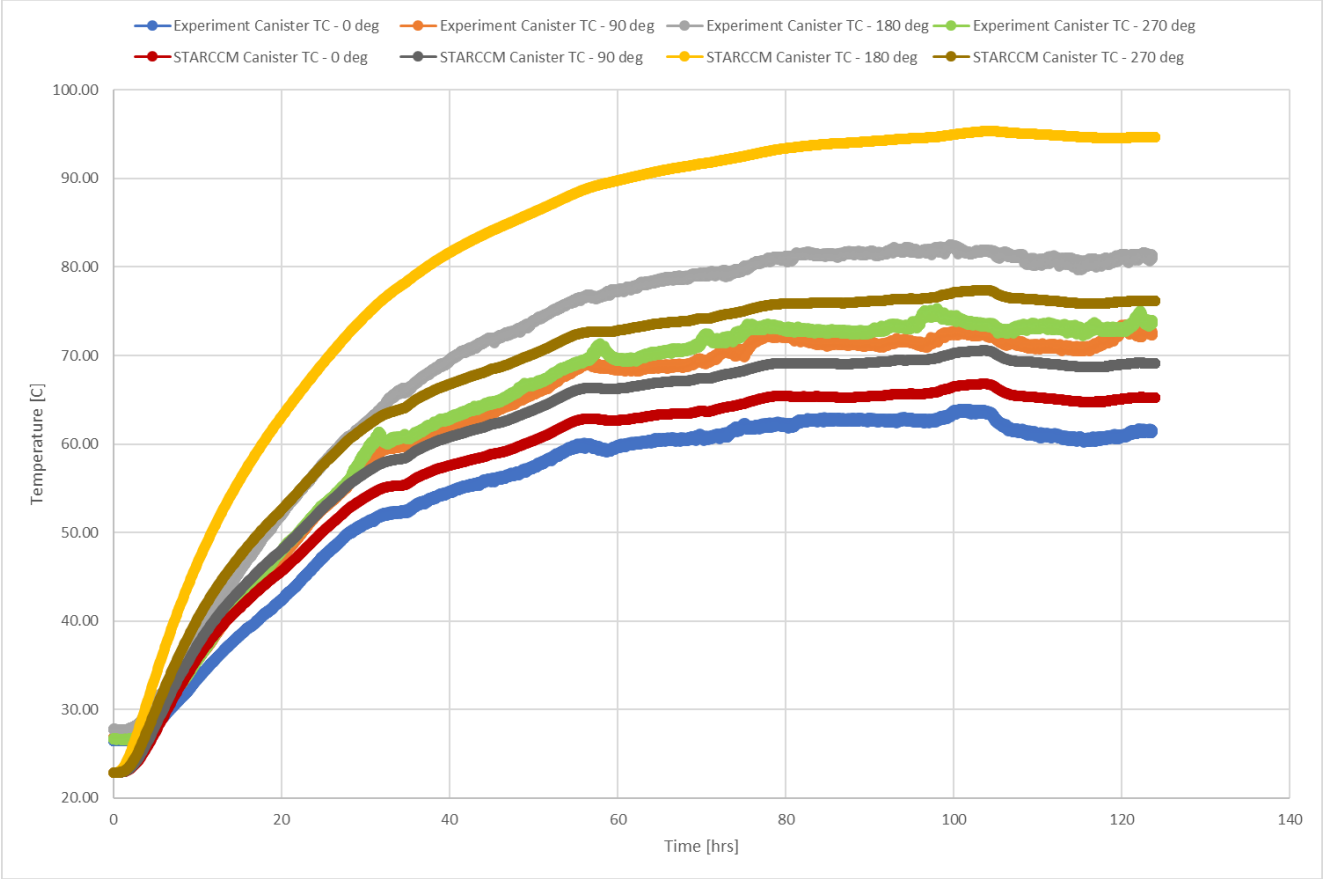

Figure 2-17. Canister Temperatures for Preliminary Heater Test at 85.375-Inch Thermocouples (Center of the Axial Heat Zone of the Canister)

This page is intentionally left blank

3. LINKAGE BETWEEN THERMAL AND DEPOITION MODELS

The PNNL STAR-CCM+ particle deposition models are built from the PNNL STAR-CCM+ thermal models. PNNL has extensive experience developing thermal models for storage and transportation canisters of SNF. Previous PNNL STAR-CCM+ thermal models have been through validation exercises such as the High Burnup Spent Fuel Data Project (Fort et al., 2019) and Dry Cask Simulator (Suffield et al., 2019 and Suffield et al., 2020). These validation exercises have provided validation and confidence in the PNNL thermal models.

The PNNL thermal models are well suited for looking at particle deposition since the flow and temperature profiles have already been set up and solved. Particle deposition is incorporated by adding particle tracking sub-models to the physics of the thermal model, creating particle injectors at the inlets and iterating the solution with particle tracking on. While the PNNL thermal models are well developed, the deposition models are preliminary and will require further development. The CDFD project will help validate the deposition models.

The CDFD project will include a no heat canister to be used as a control. It is key to limit the thermal loadings in the no heat module to limit natural convection. This will allow deposition in the no heat canister to be mainly driven by wind effects. This highlights the interplay between the thermal and deposition models.

This page is intentionally left blank.

4. DEPOSITION MODELING

This section describes preliminary particle tracking and deposition models, which were developed to predict the deposition of corrosive contaminants on SNF canisters. The modeling results shown are preliminary and for information only. The models are useful for understanding the physics of particle tracking and deposition as it applies to SNF canisters. However, they are not the final analysis of the systems discussed, and additional model development and testing will be needed before models such as these can be useful for determining the likelihood of CISCC on SNF canisters.

4.1 Background on Previous Work

During dry storage, the primary canister degradation process is likely to be CISCC at the heat-affected zones of the canister welds (NRC 2012). While it is currently unknown if there is a threshold concentration for CISCC initiation, one can assume that the onset and progress of material degradation will depend on local contaminant concentration, the properties of the contaminant species, and synergistic effects when multiple contaminants are present. The primary contaminant of concern is chloride, which is dispersed in the atmosphere and then deposits onto the canisters. Currently, the rate of chloride deposition onto the canisters is unknown. Modeling is being developed that will aid in filling this knowledge gap.

Initial PNNL deposition modeling work focused on investigating the feasibility of modeling and identifying key phenomena to include in the models. This work is documented in *Preliminary Deposition Modeling: For Determining the Deposition of Corrosive Contaminates on SNF Canisters* (Jensen et al., 2020a), and the deposition model implemented in STAR-CCM+ is referred to as the 2019 deposition model. The 2019 deposition modeling successfully demonstrated that modeling could be used to determine the rate of deposition onto canister surfaces. The 2019 modeling included implementing particle tracking into the existing PNNL thermal models and the integration of one phoretic deposition mechanism into the models. Follow on work and model development is presented in *Status Update: Deposition Modeling for SNF Canister CISCC* (Jensen et al., 2020b).

4.1.1 Deposition Forces

In the air, there are suspended solid particles and liquid droplets known as aerosols that can be transported over vast distances and for long time periods. However, the number of particles in the air is constantly changing through various mechanisms. During deposition, particles leave the air and attach to a surface. Resuspension and generation cause particles to enter the air, either by detaching from a surface or by production from a source. For the nuclear industry, a major concern is the deposition of sea-salt aerosols onto the surface of dual purpose canisters at Independent Spent Fuel Storage Installation (ISFSI) sites. Sea-salt aerosols are generally generated through the volatility of ocean water. These sea-salt aerosols can then be carried in the air to inland ISFSIs (EPRI 2015, Jensen et al., 2016). Currently, the deposition of these sea-salt aerosols onto dual purpose canisters is studied as a source for potentially initiating CISCC. In order to better understand the potential for the deposition of sea-salt aerosols onto the surfaces of dual purpose canisters, it is necessary to adequately model the mechanisms responsible for deposition within dry storage systems at ISFSIs. Potential deposition forces and mechanisms are:

- Aerodynamic deposition
- Brownian diffusion
- Diffusiophoresis
- Electrophoresis
- Gravitational settling

- Saffman lift
- Stefan flow
- Thermophoresis
- Turbophoresis
- Turbulent dispersion

A detailed description of these mechanisms is given in Jensen et al. (2020a). Aerodynamic deposition, which includes impaction and interception of a particle, and gravitational settling are included in the baseline Lagrangian particle model within STAR-CCM+.

4.1.2 2019 Deposition Model

PNNL's 2019 particle deposition model included the following surface and body particle forces:

- Drag force
- Pressure gradient force
- Gravity force
- Thermophoretic force

The thermophoretic force was implemented as a user defined body force within STAR-CCM+. The drag and pressure gradient force contribute to aerodynamic deposition, and the gravity force accounted for gravitational settling. The 2019 deposition model successfully demonstrated that modeling could be used to determine the rate of deposition onto canister surfaces. The 2019 deposition model is preliminary and was limited in the number of deposition mechanisms included.

4.2 Particle Force Sensitivity Study

A sensitivity study was run to look at the impact of additional deposition mechanisms. The additional mechanisms considered in the sensitivity study were:

- Brownian diffusion
- Diffusiophoresis
- Shear lift force
- Turbophoresis
- Turbulent dispersion

The sensitivity study was run with a simplified model to be able to efficiently run numerous cases. The AHSM-HS 32PTH2 geometry was simplified and stripped down to just the air region external to the canister and within the AHSM-HS for the simplified model. The model was also run as a half symmetry model for computational efficiency. The geometry for the simplified model is shown in Figure 4-1. The heat load was applied directly to the surface of the canister shell.

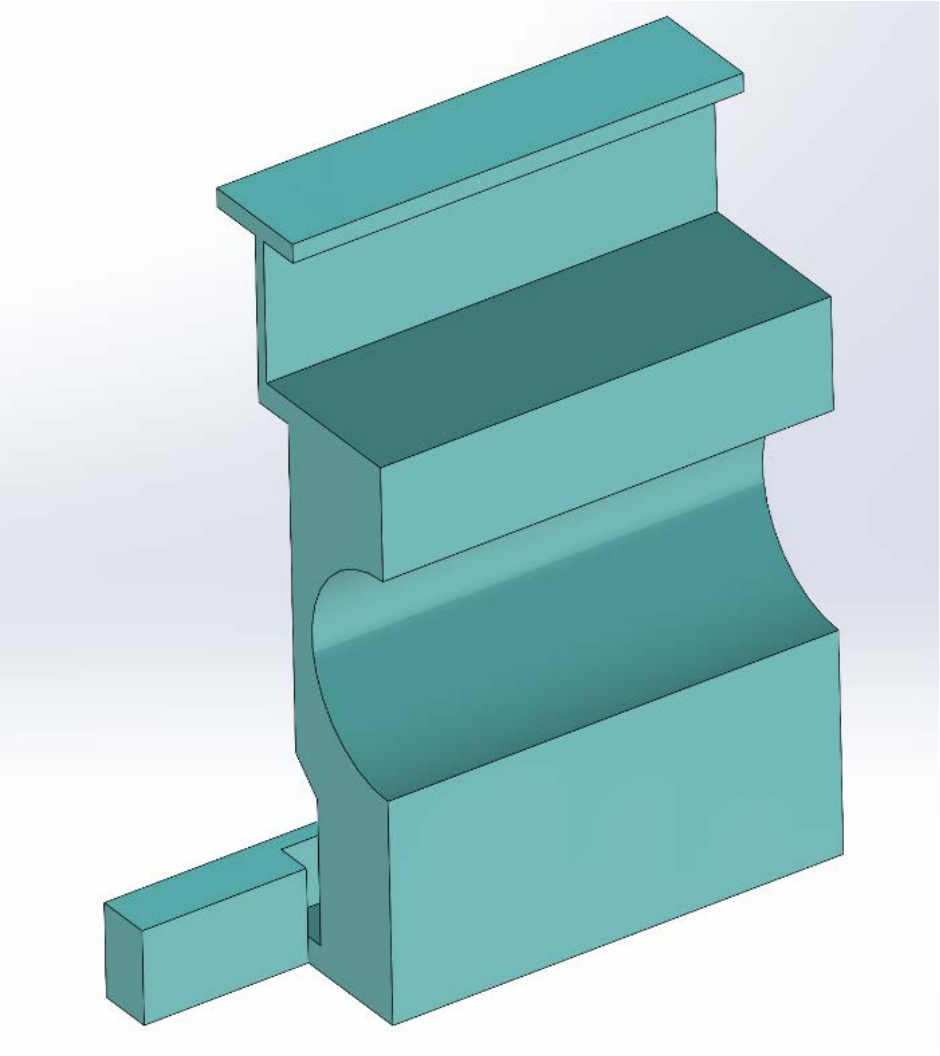

Figure 4-1. Geometry of Simplified AHSM-HS Model (only the air region external to the canister and within the AHSM-HS is modeled)

A total of 64 different cases were run for the sensitivity study. For each run the particle force was either turned on or off. All cases were run with a heat load of 10 kW, an ambient temperature of 70˚F, and a relative humidity of 61%. Droplet evaporation was not accounted for in this study (i.e., no droplet evaporation models were included). A uniform cumulative distribution function (CDF) table with particles ranging from 0.25-25 µm was used to specify the particle sizes within the STAR-CCM+ model. The results from all 64 cases were used to calculate a correlation coefficient for both canister deposition and total deposition within the overpack. The correlation coefficient is a measure of how strong a relationship there is between two variables and will have a value between -1 and 1. A value of 1 indicates a strong positive relationship between variables, a value of -1 indicates a strong negative relationship between variables, and a result of zero indicates no relationship at all. The resulting correlation coefficients are shown in Table 4-1 and Table 4-2. From the results, we see that turbulent dispersion is the most significant mechanism for deposition on the canister and within the overpack. The results also show that thermophoresis has a small negative impact on canister deposition but does not have an impact on total deposition. This makes sense since the canister is a heated surface and the thermophoretic force will cause particles to move away from warmer surfaces.

Table 4-1. Resulting Correlation Coefficients for Canister Deposition

Correlation Coefficient to Canister Deposition					
Brownian Force	**Diffusiophoresis Force**	**Thermophoresis Force**	**Turbophoresis Force**	**Turbulent Dispersion**	**Shear Lift Force**
0.00	0.00	-0.02	0.01	1.00	0.00

Table 4-2. Resulting Correlation Coefficients for Total Deposition within the Overpack

Correlation Coefficient to Total Deposition					
Brownian Force	**Diffusiophoresis Force**	**Thermophoresis Force**	**Turbophoresis Force**	**Turbulent Dispersion**	**Shear Lift Force**
0.00	0.00	0.00	0.01	1.00	0.00

4.3 Updates to the Deposition Model

The results of the particle force sensitivity analysis show that turbulent dispersion has a significant impact on deposition within the storage module. The 2019 deposition model was updated to include turbulent dispersion. A Saffman lift force was also added to the 2019 deposition model. The sensitivity study results indicate that the lift force does not have a significant impact on deposition, but this force can be easily incorporated into the STAR-CCM+ model. The implementation of turbulent dispersion and Saffman lift within the STAR-CCM+ deposition model is described in this section.

4.3.1 Turbulent Dispersion

Particles moving through a turbulent flow field will experience more dispersion than particles moving through a laminar flow field. STAR-CCM+ has a turbulent dispersion sub-model for the Lagrangian particle model. This sub-model adds a turbulent dispersion force that accounts for the interaction between the dispersed phase and the surrounding turbulent eddies (Siemens PLM Software 2021). Figure 4-2 shows the effect of the turbulent dispersion force on particles flowing through a vertical pipe. Without the turbulent dispersion force the particles do not move perpendicular to the flow from the initial injector position.

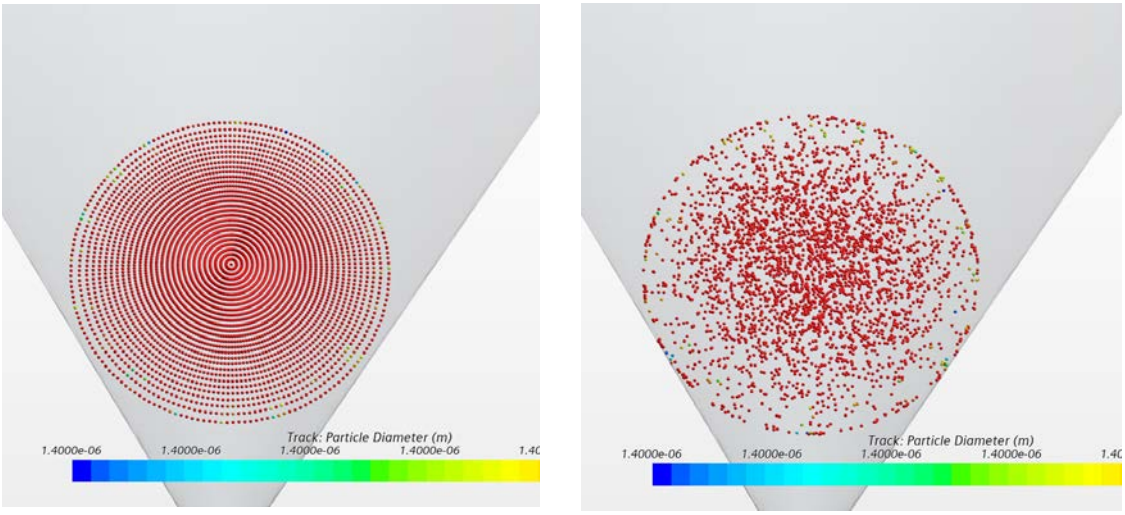

Figure 4-2. Effect of Turbulent Dispersion Force on Particles Flowing through a Vertical Pipe (a) with Turbulent Flow and No Turbulent Dispersion (b) with Turbulent Flow and Turbulent Dispersion

4.3.2 Saffman Lift

Saffman lift is the motion of a particle caused by shear force on the surface of the particle. This shear force can be caused by the particle rotating relative to the bulk flow or by a velocity gradient in the bulk flow perpendicular to the direction of flow. Depending on the relative velocities of the particle and the bulk flow, Saffman lift can result in movement either towards or away from a channel wall (Saffman 1965). STAR-CCM+ calculates the shear lift force using a shear lift coefficient and the Saffman method is a built-in option for specifying the lift coefficient (Siemens PLM Software 2021).

4.3.3 Comparisons with Validation Case

To validate the STAR-CCM+ turbulent dispersion model and Saffman lift force a simple validation model was built to simulate an experiment by Liu and Agarwal (1974). The experiment evaluated the deposition rate of aerosol particles in turbulent flow in a vertical straight pipe. The aerosol particles used in the experiment were uniform spherical droplets of olive oil containing a florescent tracer that was less than 10% by weight. The amount of tracer deposited on the walls was measured along a 102 cm long glass tube. The tube had a 1.27 cm inner diameter. A STAR-CCM+ model was constructed to simulate the experiment. A simple geometry of the air flowing through the vertical pipe was constructed in SolidWorks. The CAD geometry was imported into STAR-CCM+ and meshed. A 0.1 cm thick prism layer boundary with 20 cell layers was applied along the inner wall of the pipe. This ensured a wall y+ value of less than 1 along the wall. A radial cross-section of the mesh, taken through the center of the vertical pipe, is shown in Figure 4-3.

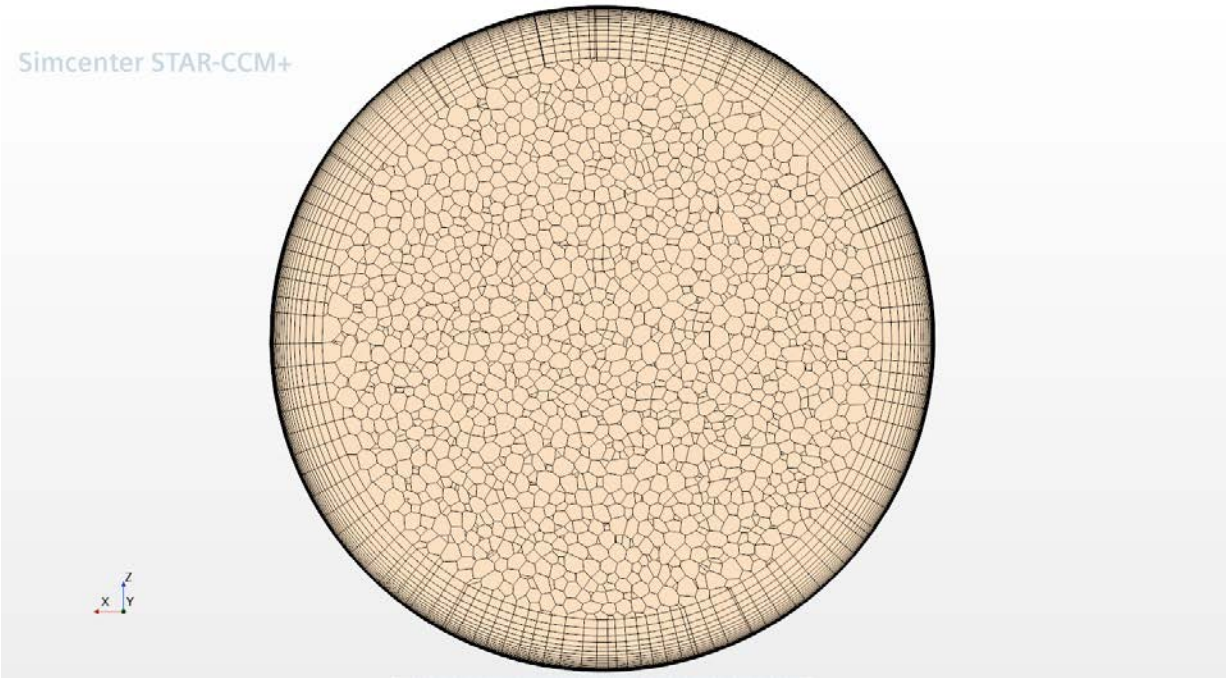

Figure 4-3. CAD Geometry of Simple Turbulent Deposition Validation Model

Deposition was measured from 12.75 cm to 63.75 cm, with 0 cm corresponding to the bottom of the pipe, to match the region measured and reported in the experiment (Liu and Agarwal 1974). A mesh sensitivity was run to ensure that the mesh was properly resolved to capture deposition along the walls. The mesh sensitivity runs used a Reynolds number (Re) of 10,000 and a particle diameter of 21 µm. Figure 4-4 shows the results of the mesh sensitivity. A core mesh size of 0.25 mm was found to be sufficiently resolved.

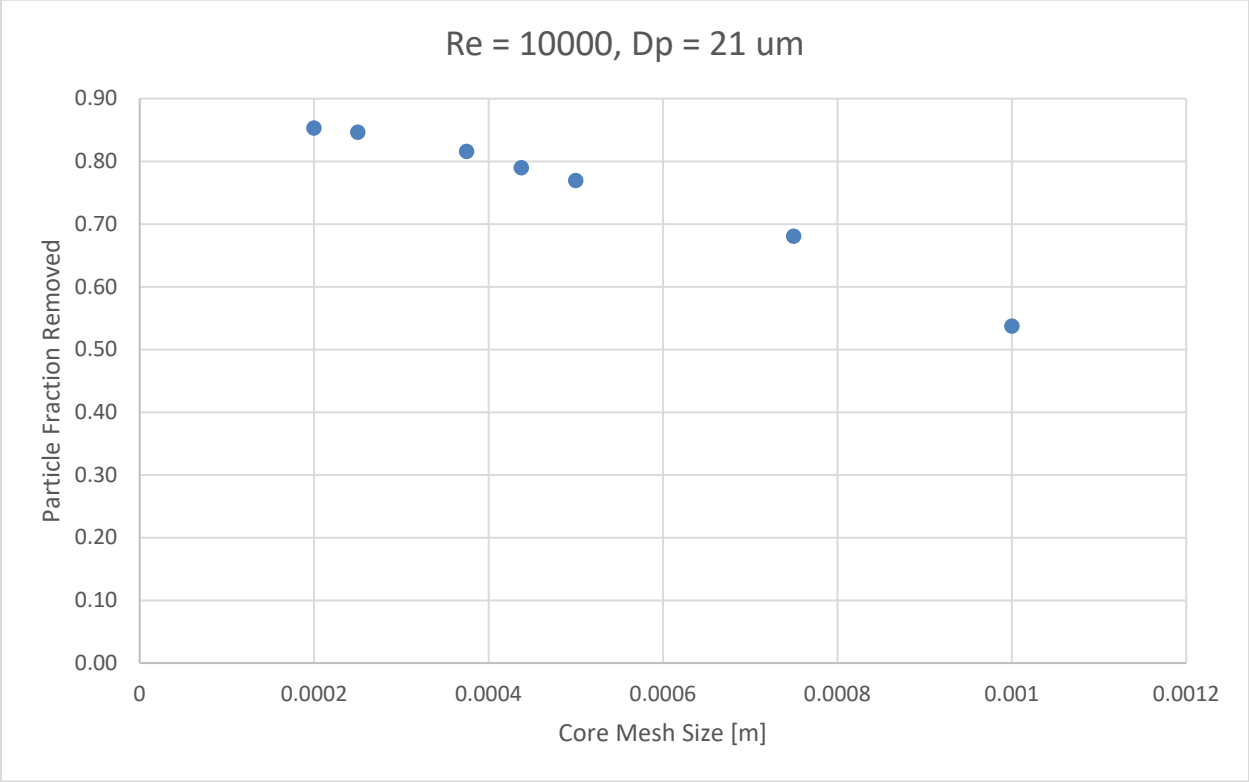

Figure 4-4. Core Mesh Sensitivity Study for Simple Turbulent Deposition Validation Model

The model was run at Reynold numbers of 10,000 and 50,000, and at different particle diameters ranging from 1.4-21 µm to match test conditions run by Liu and Agarwal (1974). A total of 5000 particles were injected at the tube inlet of the model. The STAR-CCM+ model was run with the updated particle deposition model that included the addition of turbulent dispersion and Saffman lift. Results are shown in Figure 4-5.

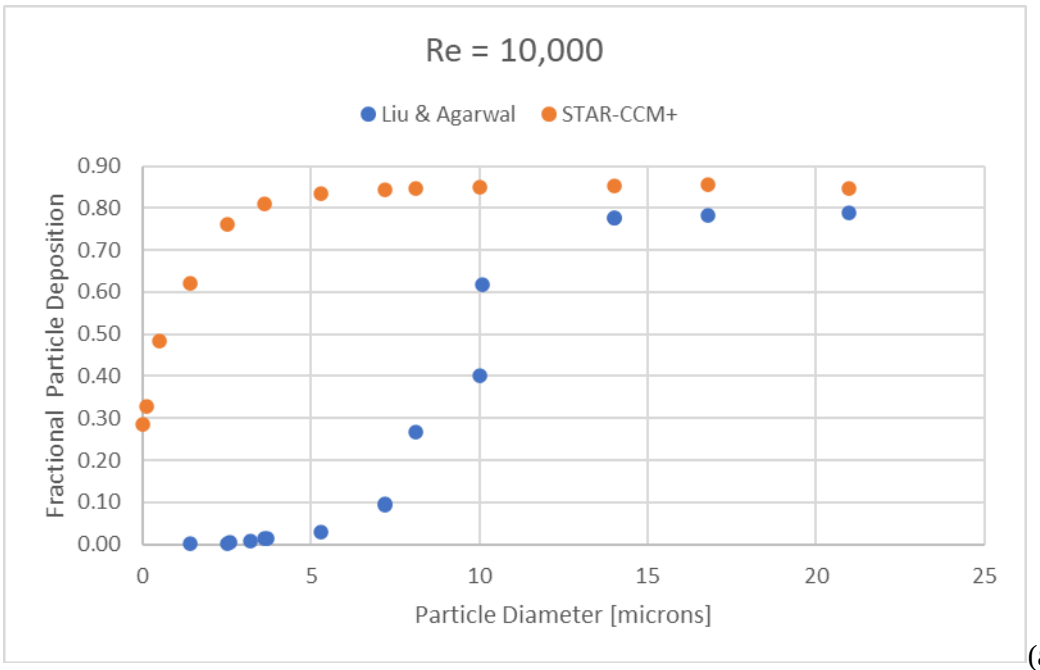

(a)

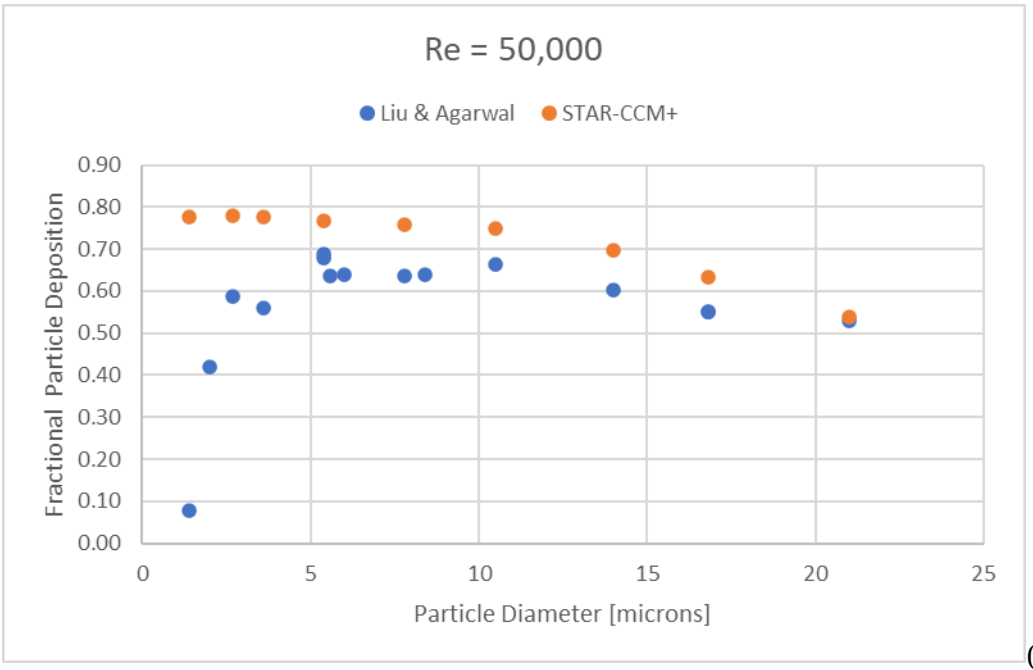

(b)

Figure 4-5. Particle Deposition for Initial Turbulent Deposition Validation Model for (a) 10,000 Reynolds Number Case and (b) 50,000 Reynolds Number Case

The results show that the STAR-CCM+ model is significantly overpredicting deposition for the smaller particles. These results seem consistent with others who have modeled this problem in commercial CFD codes. Tang and Guo (2011) point to other authors that had found the RANS turbulent dispersion and deposition model as not adequately accounting for dampening of the turbulent fluctuation normal to the wall and would over predict the particle deposition on the wall.

4.3.4 Wall Correction Factor

The RANS turbulent models within STAR-CCM+, including the k-omega SST model, treat the near wall turbulent fluctuation velocity as isotropic but in reality it is anisotropic. This causes the RANS turbulent dispersion and deposition model to not adequately account for dampening of the turbulent fluctuation normal to the wall and over-predicts the particle deposition on the wall for smaller particles. To correct this overprediction, a damping correction factor will be applied in the near wall region, normal to the wall given by Wang and James (1999):

$$f_v = 1 - \exp(-0.02y^+)$$

The damping correction factor is multiplied by the turbulent fluctuation velocity normal to the wall. To apply this to the steady state STAR-CCM+ model a user defined opposing particle force was specified in the near wall region, in the direction normal to the wall, based on the damped velocity:

$$F_{wall\_correction} = \frac{-6\pi\mu\frac{d_p}{2}u_n'(1-f_v)}{V_p C}$$

Where;

d_p = particle diameter

u'_n = turbulent fluctuation velocity in the direction normal to the wall

μ = dynamic fluid viscosity

V_p = particle volume

C = Cunningham correction factor

The wall correction particle force was implemented into the STAR-CCM+ turbulent deposition validation model. The force is only applied in the near wall region along the first few prism layer cells. The results of the model updated with the wall correction force are shown in Figure 4-6. Overall, the deposition of the small particles in the STAR-CCM+ model compare much better with the particle dampening force applied.

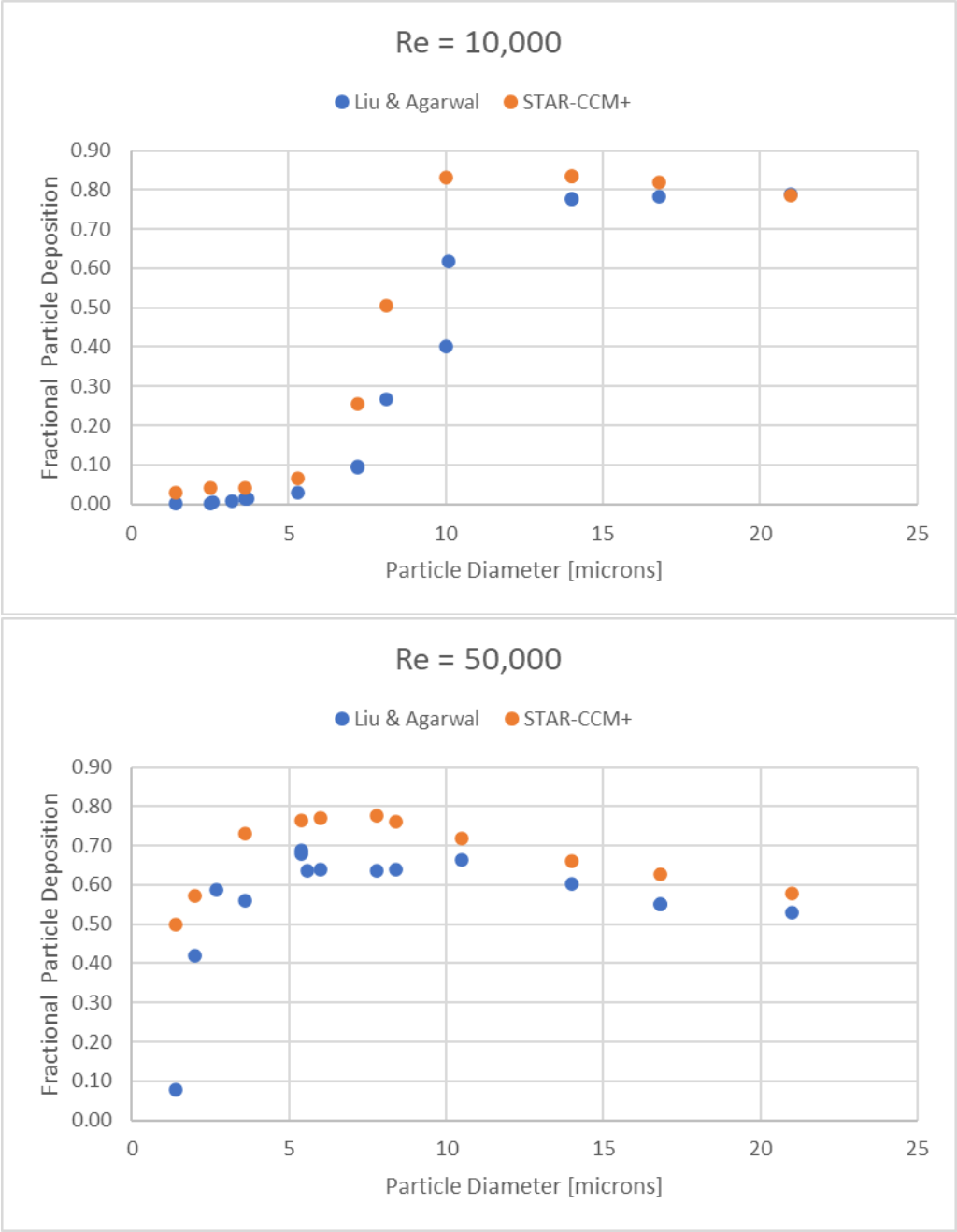

Figure 4-6. Particle Deposition for Updated Turbulent Deposition Validation Model with a Wall Correction Force Applied for (a) 10,000 Reynolds Number Case and (b) 50,000 Reynolds Number Case

4.4 Standalone Deposition Models

The deposition model was incorporated into the PNNL STAR-CCM+ thermal models of the AHSM-HS 32PTH2 with SNF. Initially the 2019 particle model was integrated into the models. An updated particle model, referred to as the 2021 particle model, added turbulent dispersion, Saffman lift, and a wall correction force to the particle mechanisms already included in the 2019 model. A uniform CDF table with particles ranging from 0.25-25 µm defined the particle sizes injected at the inlets of the STAR-

CCM+ model. Details and results from the standalone deposition models (no external environment) are presented in this section.

4.4.1 Single AHSM-HS Model

The 2019 particle model was integrated into the baseline thermal model described in Section 2.1.5. An injector sensitivity study was run to determine the number of injectors required to accurately capture the deposition. The deposition efficiency was calculated by dividing the total particle mass at a surface, or surfaces, by the total particle mass injected at the inlets. The injectors are placed at the inlets of the AHSM-HS in the standalone model. A part injector and surface injector set at the inlets were used in the sensitivity study. Both the part and surface injector placed injectors at the centroid of the cell faces on the inlets. A unique feature of the surface injector is that the mass of each parcel is proportional to the area of the face from which it came from. The part injector assumed a uniform mass distribution across all cells. The number of injectors was controlled by refining the mesh at the inlets. Results of the injector sensitivity study are shown in Figure 4-7. The case with the lowest number of injectors was run with a part injector. All other cases used a surface injector. The results show that a count of around 2000 injectors was adequate. This corresponds to around 1000 injectors per inlet (there are two inlets per AHSM-HS). A target surface element of 1 inch (2.54 cm) corresponded to approximately 1000 injectors per inlet. A uniform CDF table with particles ranging from 0.25-25 µm defined the particle sizes injected at each inlet.

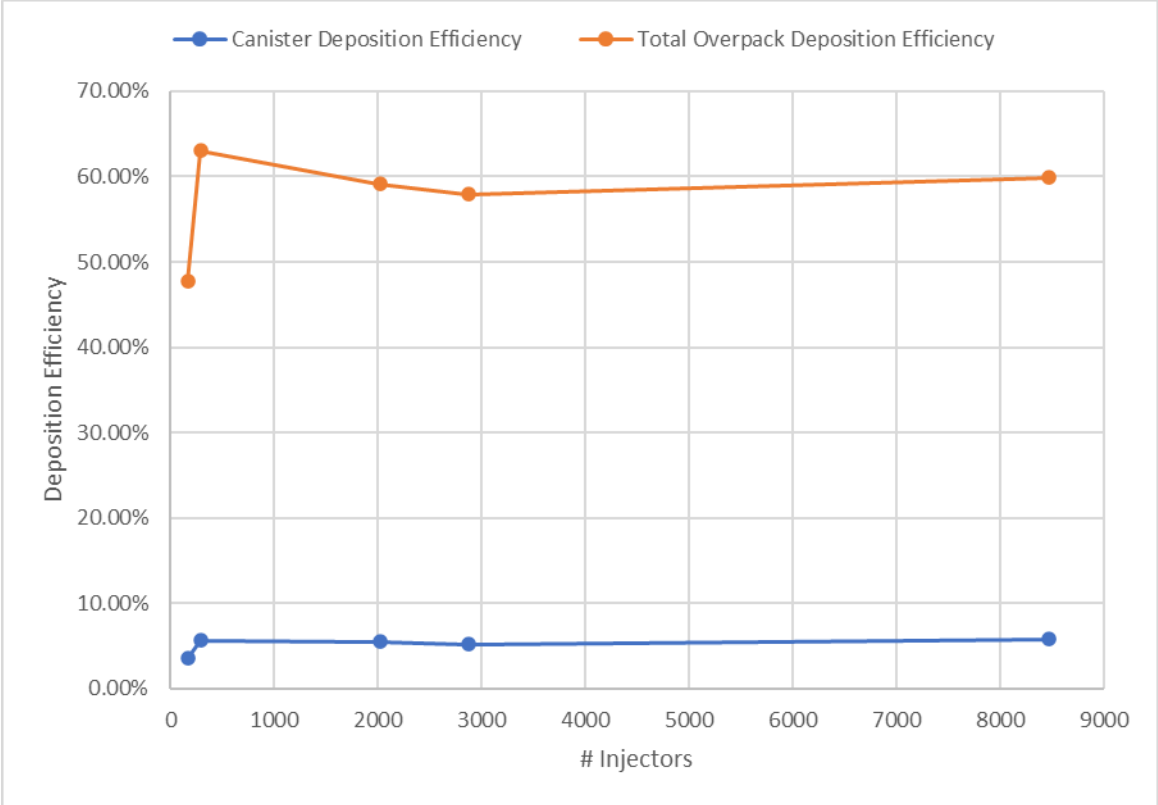

Figure 4-7. Injector Sensitivity Study with Single AHSM-HS Model and the 2019 Particle Model

The single standalone AHSM-HS model was updated with the 2021 particle deposition model. The model was run with an average ambient temperature of 75.7˚F (16.1˚C) to represent a typical yearly average temperature of a marine coastal site. The model was run for the three different heat load configurations: the high heat load of 40 kW, the low heat load of 10 kW, and the no heat canister. In the standalone single AHSM-HS model with no heat load the flow is driven exclusively by the solar loadings. Results are shown in Table 4-3. These results are preliminary, and the deposition efficiency is calculated based on particle mass. The particle mass does not change as the particles travel through the overpack. Future work will add droplet evaporation to the STAR-CCM+ particle model, and the particle size and mass will change depending on the local relative humidity within the overpack. The deposition efficiency calculation will need to be re-evaluated with the addition of droplet evaporation.

Table 4-3. Preliminary Deposition Results for Standalone Single AHSM-HS 32PTH2 Model

Model	Total Heat Load [kW]	Inlet Mass Flow [kg/s]			Total Deposition Efficiency[1]	Canister Deposition Efficiency[1]		
		High Heat AHSM-HS	No Heat AHSM-HS	Low Heat AHSM-HS		High Heat Canister	No Heat Canister	Low Heat Canister
Single AHSM-HS Module with 2021 Particle Model	40	0.81	-	-	77.41%	8.34%	-	-
Single AHSM-HS Module with 2021 Particle Model	0	-	0.24	-	73.30%	-	6.35%	-
Single AHSM-HS Module with 2021 Particle Model	10	-	-	0.53	77.53%	-	-	9.00%

1. Deposition efficiency represents the fraction of particle mass deposited on surfaces versus the total particle mass injected at the inlets.

4.4.2 Three AHSM-HS Model

Particle deposition was integrated into the three AHSM-HS 32PTH2 thermal model described in Section 2.1.6. The 2019 and 2021 particle models were run with the three AHSM-HS model. The 2021 particle model was run both with and without the wall correction force to look at the sensitivity to this correction in the SNF storage model. Results are shown in Table 4-4 and Figure 4-8. The canister deposition results shown for the 2021 deposition model in Figure 4-8 include the wall correction particle force. All results are preliminary.

Table 4-4. Preliminary Deposition Results for the Standalone Three AHSM-HS 32PTH2 Model

Model	Total Heat Load [kW]	Inlet Mass Flow [kg/s]			Total Deposition Efficiency[1]	Canister Deposition Efficiency[1]		
		High Heat AHSM-HS	No Heat AHSM-HS	Low Heat AHSM-HS		High Heat Canister	No Heat Canister	Low Heat Canister
3 AHSM-HS Modules with 2019 Particle Model	50	0.81	0.23	0.53	55.85%	1.76%	4.94%	3.54%
3 AHSM-HS Modules with 2021 Particle Model with No Wall Correction	50	0.81	0.23	0.53	86.00%	10.12%	6.00%	10.22%
3 AHSM-HS Modules with 2021 Particle Model with Wall Correction	50	0.81	0.23	0.53	81.61%	8.13%	6.33%	8.07%

1. Deposition efficiency represents the fraction of particle mass deposited on surfaces versus the total particle mass injected at the inlets.

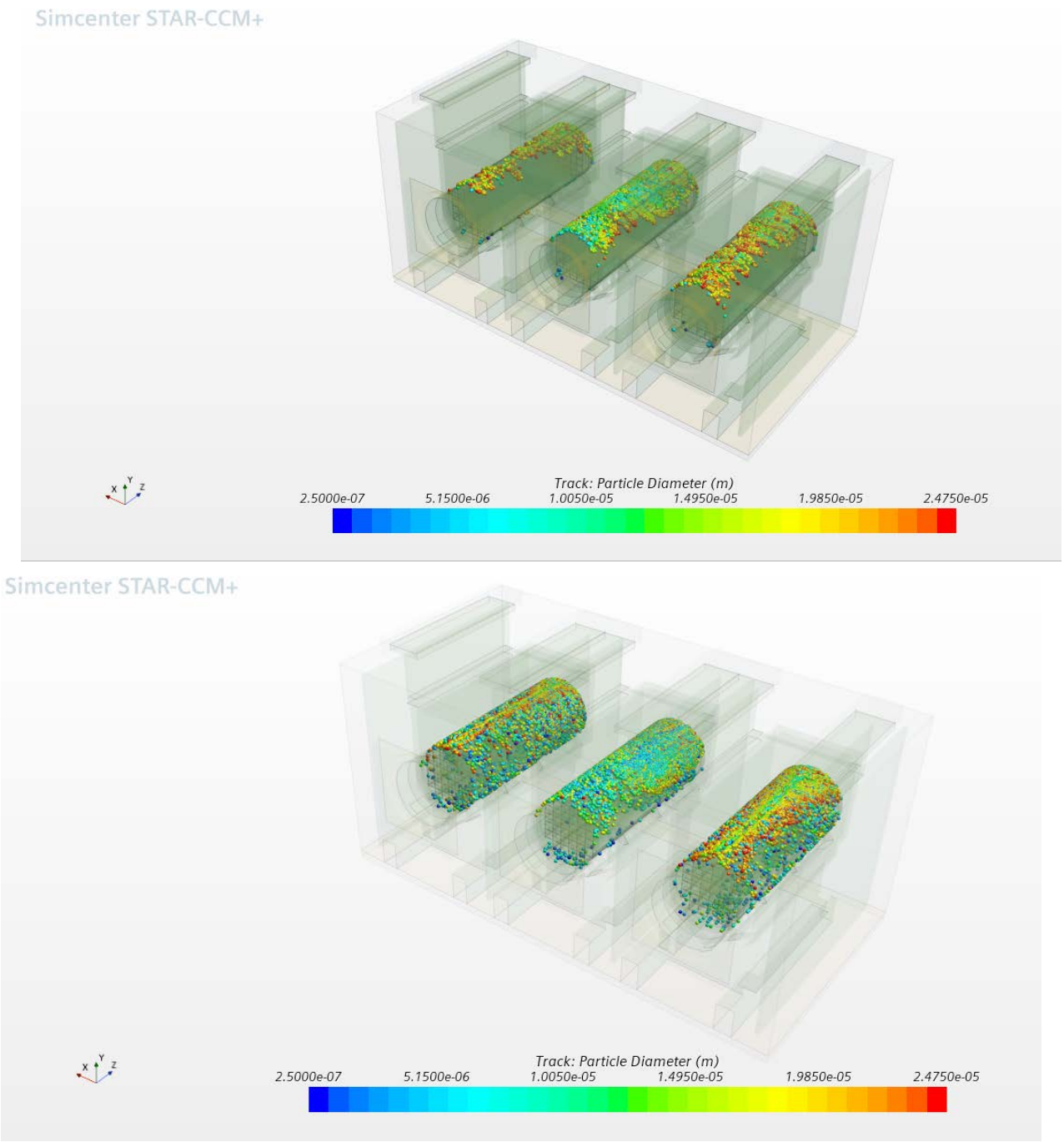

Figure 4-8. Canister Deposition Results for Standalone Three AHSM-HS 32PTH2 Model with (a) 2019 Deposition Model and (b) 2021 Deposition Model. Canister temperature distribution shown in Section 2.1.6. PRELIMINARY

The results show smaller particles depositing on the center, no heat canister. The results also show that the updated 2021 deposition model increased deposition on the canister surface, especially for the heated canisters. This makes sense since the heated canisters will have more turbulent flow driven through those modules for the natural convection case (no wind). Figure 4-9 plots the turbulence intensity through a

radial cross-section of the AHSM-HS modules versus canister deposition, which shows a region of higher turbulence intensity at the top of each canister that drives deposition in all three modules. A comparison of the turbulence intensity through the center of the high heat and no heat canister versus canister deposition is shown in Figure 4-10. The high heat canister plot shows significantly more turbulence intensity, especially along the bottom of the canister which corresponds to more deposition along the bottom of the canister than the no heat canister.

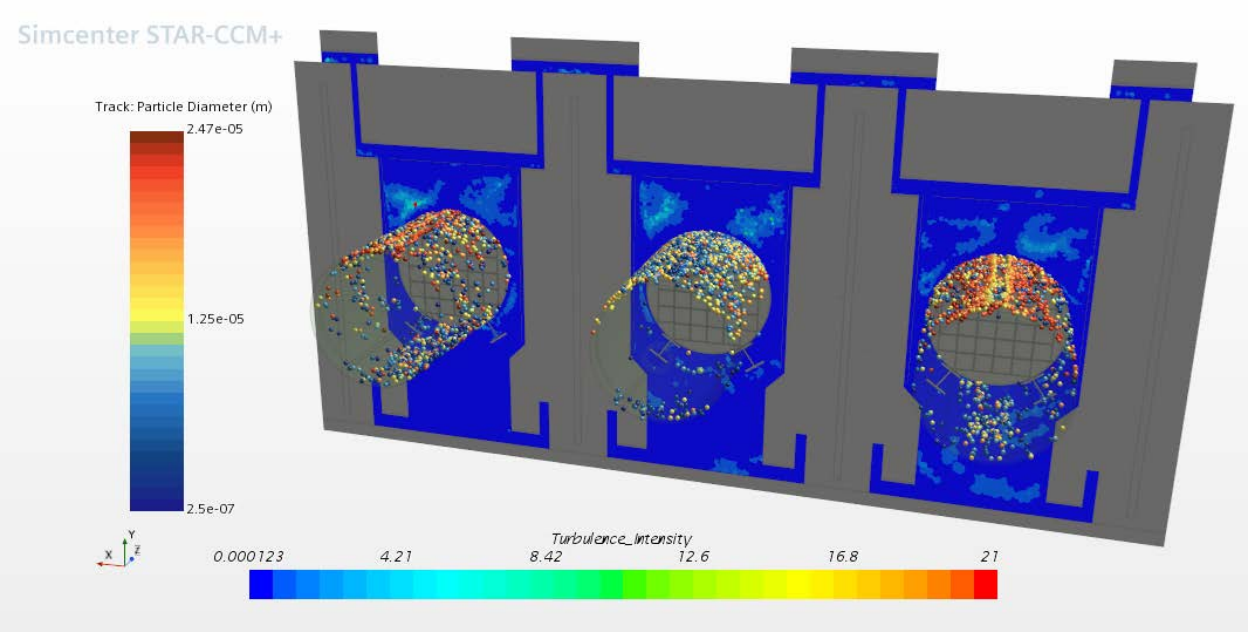

Figure 4-9. Turbulence Intensity Versus Canister Deposition through a Radial Cross-section of the Standalone Three AHSM-HS Model

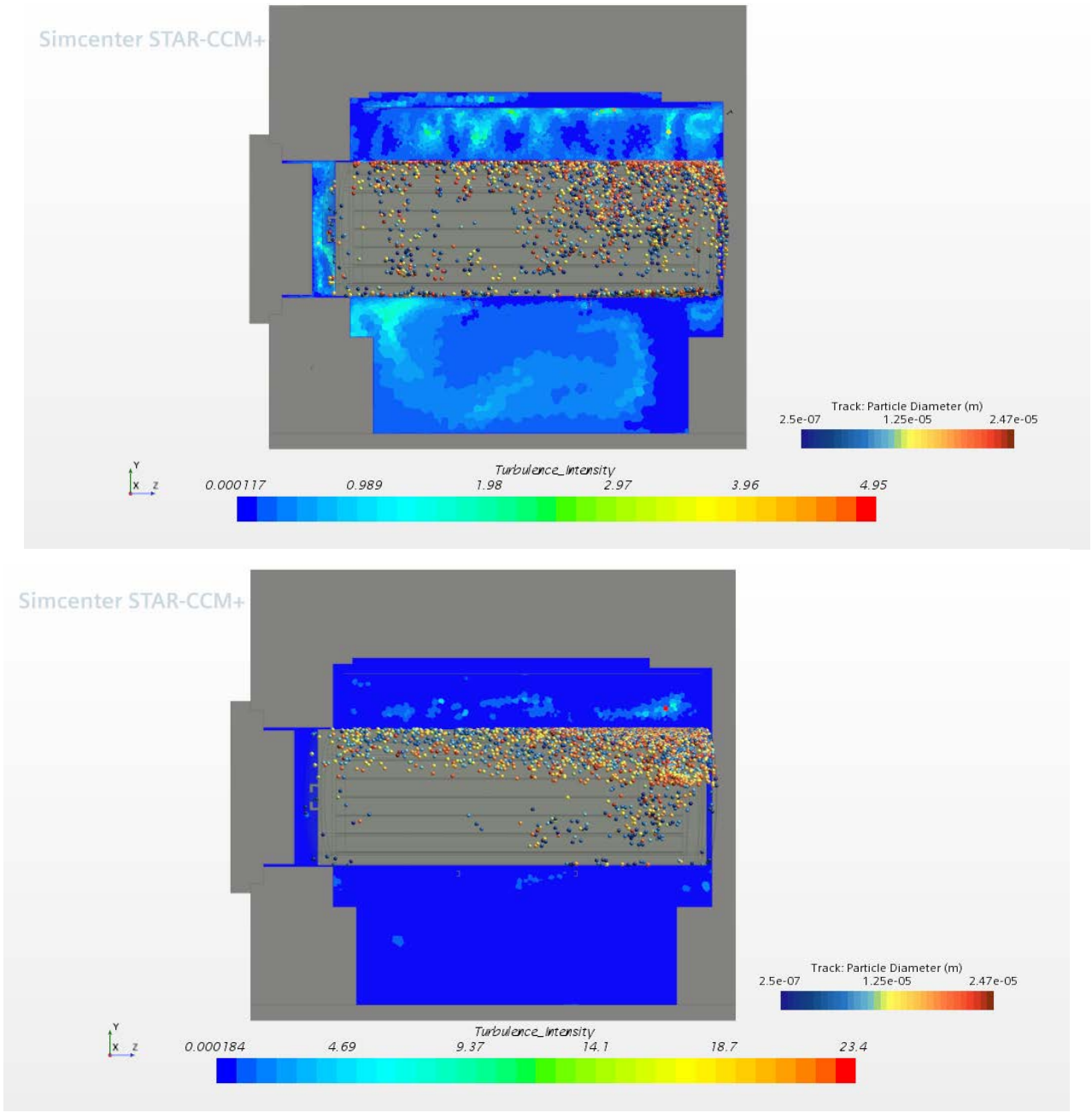

Figure 4-10. Turbulence Intensity Versus Canister Deposition through an Axial Cross-section of the Standalone Three AHSM-HS Model for the (a) High Heat Module and (b) No Heat Module

The 2021 particle deposition model that includes the addition of turbulent dispersion, Saffman lift, and the wall correction force will be used in future deposition models.

4.4.3 Comparisons Between Single and Three AHSM-HS Model

Table 4-5 compares the deposition results for the single and three AHSM-HS standalone models. The results show that the three AHSM-HS model and single models compare very well. This further indicates that the intermediate wall is adequately isolating the thermal loads from neighboring modules.

Table 4-5. Comparison of Deposition Results for Single and Three AHSM-HS Standalone Models

Model	Total Heat Load [kW]	Inlet Mass Flow [kg/s]			Canister Deposition Efficiency[1]		
		High Heat AHSM-HS	No Heat AHSM-HS	Low Heat AHSM-HS	High Heat Canister	No Heat Canister	Low Heat Canister
3 AHSM-HS Modules with 2021 Particle Model	50	0.81	0.23	0.53	8.13%	6.33%	8.07%
Single AHSM-HS Module with 2021 Particle Model	40	0.81	-	-	8.34%	-	-
Single AHSM-HS Module with 2021 Particle Model	0	-	0.24	-	-	6.35%	-
Single AHSM-HS Module with 2021 Particle Model	10	-	-	0.53	-	-	9.00%

1. Deposition efficiency represents the fraction of particle mass deposited on surfaces versus the total particle mass injected at the inlets.

4.4.4 Solar Loading Sensitivity Case

A sensitivity case was run with the standalone three AHSM-HS deposition model to verify that the natural convection flow in the no heat canister is driven by solar loadings. The sensitivity case was run with no heat to any of the three modules. This left the solar loads as the only active thermal loads. Results are shown in Table 4-6 and show that with no heat load for any of the canisters the deposition is approximately equal among the three canisters. This verifies that the natural convention model is driven by solar loadings in the no heat control canister.

Table 4-6. Solar Loading Sensitivity Case with Standalone Three AHSM-HS 32PTH2 Model

Model	Total Heat Load [kW]	Inlet Mass Flow [kg/s]			Canister Deposition Efficiency[1]		
		High Heat AHSM-HS	No Heat AHSM-HS	Low Heat AHSM-HS	High Heat Canister	No Heat Canister	Low Heat Canister
3 AHSM-HS Modules with 2021 Particle Model	0	0.21	0.21	0.20	6.27%	6.51%	6.60%

1. Deposition efficiency represents the fraction of particle mass deposited on surfaces versus the total particle mass injected at the inlets.

4.5 Wind Effects Deposition Models

Particles were added into the wind effect models described in Section 2.1.5. The main goal of the wind effects model is to understand what percentage of particles make it into the AHSM-HS modules. The 2019 deposition model was initially integrated into both the single and three AHSM-HS wind effect models. The three AHSM-HS model was updated with the 2021 deposition model. Preliminary particle flow and deposition model results are presented in this section.

4.5.1 Single AHSM-HS Wind Effects Model and Particle Injector Sensitivity Analysis

The single AHSM-HS wind effects model from Section 2.1.7.2 is used for particle deposition studies. The particle deposition model used for this single assembly wind effects model is based in the 2019 model described in Section 4.1.2. This single AHSM-HS wind effects model was used for determining the best strategy for injecting particles to model particle flow and deposition.

To accurately model external particle flow into and around the AHSM-HS, a strategy for injecting particles into the external environment is necessary. The objective is to efficiently model well-dispersed particles (dust clouds often seen on windy days, sea salt spray/mist, etc.) in external wind flow for SNF casks using STAR-CCM+. This enables realistic modeling of the external environment around the SNF dry storage system, as well as the system itself. The main difficulty in modeling well mixed particles is balancing computational expense with accurately capturing the dispersed particles. In STAR-CCM+ particles are injected on discrete points in the model. To manage the computation expense, this study focuses on determining the best far field injection strategy to capture particles entering the AHSM-HS storage system. There are a variety of ways to introduce particles into a flow domain in STAR-CCM+ that are relevant to this application, these are:

- Hollow Cone Injector
- Part Injector
- Point Injector
- Solid Cone Injector
- Surface Injector
- Table Injector

For this application the part/surface, and table injectors have the most potential. The other injector types are not very well suited to study. The point and cone injectors are not well suited because they introduce particles at one point that are difficult to spread out, which is not very representative of well-dispersed particles in air. One method is to introduce multiple cone injectors through the cone injector and adjust the particle injection velocity to spread out the particles for a part injector. An issue with that method is that it will spread out larger heavier particles further than the smaller lighter ones, which introduces a bias. The most promising injector types introduce a user specified number of injection points over an area and are easily configured to cover a specified area. The best particle injection strategy will be easily configured to the desired geometry and injection point density.

For this study, a part injector forming square, evenly-spaced injection points over a grid and a table injector forming random injection points were selected. These injection patterns are shown in Figure 4-11 and Figure 4-12. The table injector is configured by specifying the x,y,z coordinates of each injection point in a table that is read by STAR-CCM+. Both methods are easily user configurable for the shape of the injection area and injection point density.

The table injector and grid part injector are the two best particle injection methods for this application. To evaluate and verify the table injector method, 30 trials of different randomly distributed injection points

for 100pts, 1,090pts, and 10,000pts over a 39.69 m^2 area are run. This comes out to 2.5, 25.2, and 252.0 injection points per m^2. These randomly distributed particle injection point strategies are shown in Figure 4-11. For this condensed injection area, many particle streams still fly by without hitting the inlet or interacting with the cask, so to ensure the solution is independent of the coverage area (as long as the injection grid provides sufficient coverage of the cask) the number of particles entering the cask is normalized. These 30 trials are analyzed by calculating the minimum, maximum, mean, and standard deviation of the particle entrance efficiency. Particle entrance efficiency is the number of particles injected per injection area divided by the number of particles entering the cask per inlet area. The main objective is to show the variation between trials of the same number of particle stream injection points decreases as the particle stream injection point density increases. Smaller variation between the random trials indicates the particle density is such that the coverage of particles is sufficient to accurately determine the particle entrance efficiency in the cask system.

In addition to the table injector method, the presentation grid method is used for 2.5pts/m^2 (100pts), 25.2pts/m^2 (~1090pts), and 252.0 pts/m^2 (10,000pts). The resulting particle entrance efficiencies are compared with the mean from the random table injector runs. These grid particle injection points are shown in Figure 4-12. For the 25.2pts/m^2 case, the injection area and number of injection points were adjusted slightly to maintain the particle stream injection point density. The solution is independent of the absolute injection area and particle count.

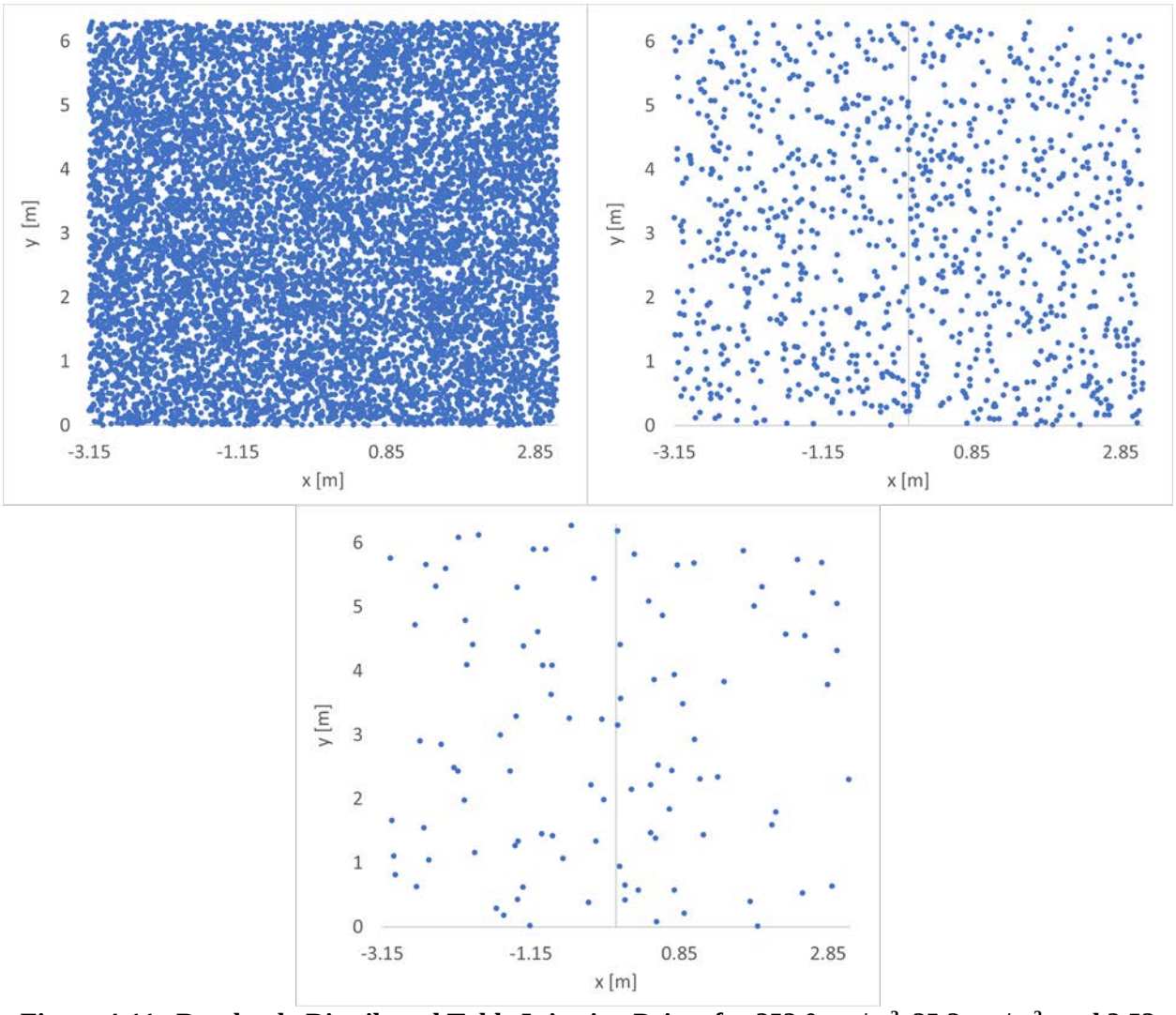

Figure 4-11. Randomly Distributed Table Injection Points for 252.0 pts/m^2, 25.2 pts/m^2, and 2.52 pts/m^2

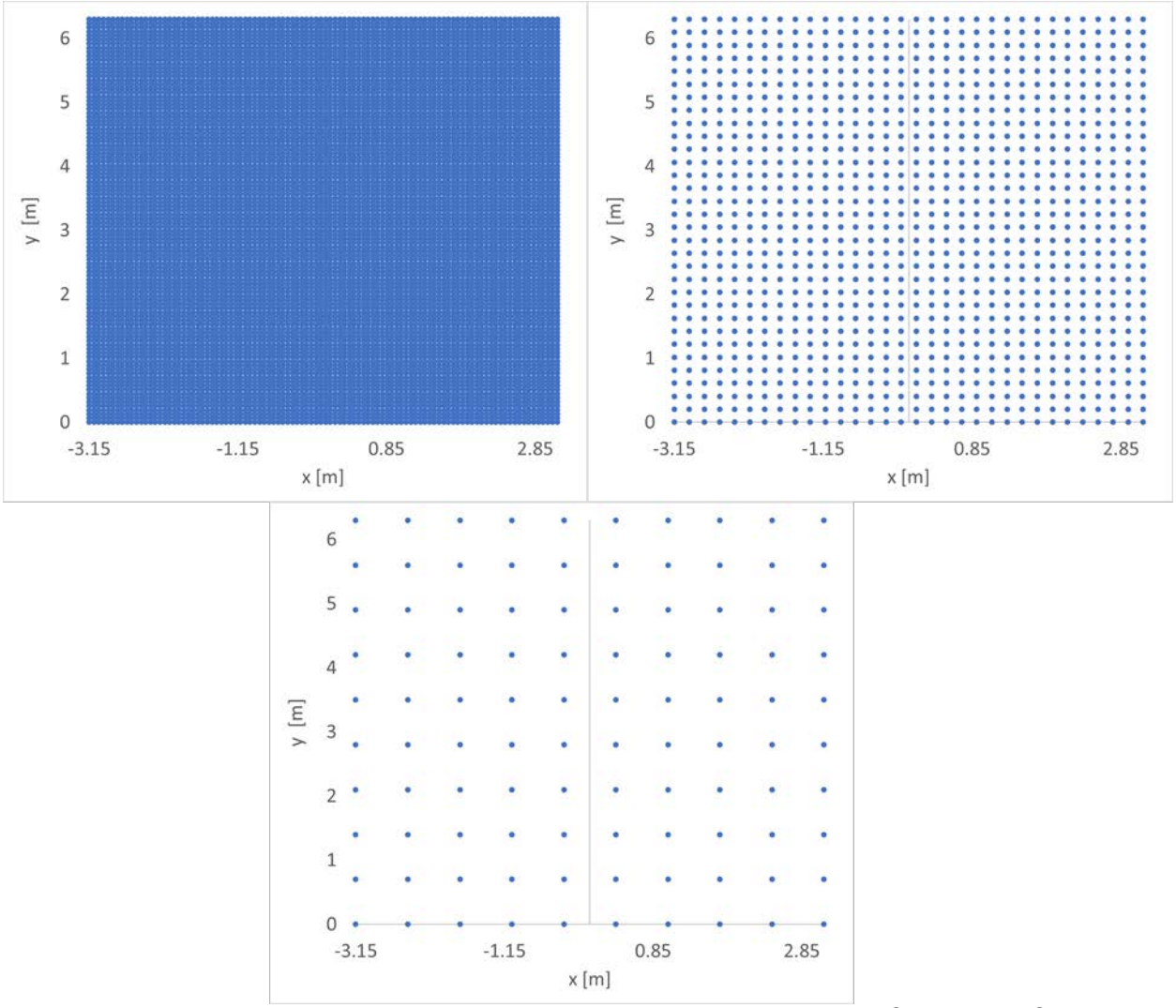

Figure 4-12. Grid Distribution of Particle Injection Points, for 252.0 pts/m^2, 25.2 pts/m^2, and 2.52 pts/m^2

The particles used for this study are unchanged from the 2019 particle deposition model (Jensen et al., 2020a). The particles range in diameter from 0.5 μm to 25.0 μm uniformly distributed and have the approximate density of water. The deposition model used for this exercise is the 2019 model. The focus of this study was on particle injector sensitivity and best practices that could be applied to any deposition models. These different particle injection point distributions and densities were all tested using the same windspeed and direction. The windspeed is configured to be 5.0 m/s normal to the inlets of the cask.

The heat load inside the canister is turned off. This is a negligible impact because at the wind speed and direction used for this exercise, the flow through the cask is dominated by the wind rather than natural convection (Jensen et al., 2020b).

Table 4-7 shows the results of the 30 random trials for each particle injection point density. The standard deviation decreases as the particle injection point density increases. This is also indicated by the difference between the maximum and minimum particle entrance efficiency with higher injection point density.

For the trials with 2.5 pts/m^2, multiple trials failed to track any particles hitting the inlet, resulting in 0% entrance efficiency. Other trials grossly overestimated entrance efficiency with efficiencies of over 100%.

This is most likely due an insufficient number of injection points needed to accurately represent the particle injection point density. Particle entrance efficiency could also go above 100% due to geometry, fluid flow, and steady state particle tracking. A single particle stream carries much more weight (higher particle count per stream) at the lower particle injection point densities. These concentrated number of particles on the particle streams leads to either grossly over- or under-predicting the particle entrance efficiency. With a small number of injection points/particle streams the efficiency entering the inlet is particularly sensitive.

For all three particle injection point densities the average efficiency of inlet particle entrance is very close. This means for the lower particle injection point densities, the over- and under-prediction averages itself out to what is a stable solution. Averaging out 2.5 pts/m^2 runs is similar to adding more injection points.

The standard deviation for the 25.2pts/m^2 and 252.0 pts/m^2 is significantly less than for the 2.5 pts/m^2 case. 95% of the trials for the 252.0 pts/m^2 case are within about ±10% for the mean entrance efficiency where the 25.2 pts/m^2 case 95% of the trials are within ±26% for the mean entrance efficiency. Depending on application, 252.0 pts/m^2 provides a reasonable estimation for particle entrance efficiency in SNF casks for external wind applications. Using this method of running trials of randomly distributed points enables error analysis and establishes confidence in a single solution.

Table 4-7. Particle Entrance Efficiency Results for the Randomly Distributed Injection Points

	2.5pts/m^2 [%]	25.2pts/m^2 [%]	252.0pts/m^2 [%]
Min	0.00	15.84	26.26
Max	143.55	64.14	48.09
Average	40.67	42.64	41.09
Std. dev.	40.44	13.09	5.44

Along with the random particle injectors, grid injection points used in the previous report from Jensen et al. (2020b) were analyzed. The objective of this analysis is to compare the grid injection pattern to the random injection grids. The grids consist of 2.5pts/m^2 (10x10), 25.2 pts/m^2 (33x33 over adjusted area to maintain injection point density), 252.0 pts/m^2 (100x100). Table 4-8 shows the results of the particle entrance efficiency. It appears that the particle entrance efficiency is close to the averages for the trials of randomly distributed injection points for the 25.2 pts/m^2 and 252.0 pts/m^2 presentation grids. The 2.5 pts/m^2 case is plagued by the same under-prediction that was seen with the randomly distributed trials. One take away from this is that 2.5pts/m^2 is not enough particle injection points to accurately capture the particles from the far boundary to the cask. It appears that 25.2 pts/m^2 in a grid has enough points to accurately capture the particle entrance efficiency as the efficiency prediction is very close to the average predictions in the previous 25.2pts/m^2 and 252.0pts/m^2 random grid trials. There is still a larger uncertainty with using 25.2pts/m^2 in a grid than with using 252.0 pts/m^2 in a grid. For the grid injector the even distribution of injection points works to its advantage ensuring a consistent distribution of particles across the injection area, which is a possible contribution to the efficiency of this method in predicting particle entrance efficiency. With the random table injector method, injection points can be clumped together depending on the randomness of the distribution.

Table 4-8. Grid Particle Entrance Efficiency Results

	2.5 pts/m^2 [%]	25.2 pts/m^2 [%]	252.0 pts/m^2 [%]
AHSM-HS	0.00	41.73	41.70

After considering the results from analyzing both the randomly distributed and grid injection, using 25.2pts/m^2 in a presentation grid is the most efficient way to model particle entrance into spent nuclear fuel casks in external wind cases. In all cases it is better to use more points, but when computation expense is of particular importance, 25.2pts/m^2 in a grid is sufficient when accompanied by spot verification with a higher injection point density. When looking at the 252.0pts/m^2 density cases, we see the grid distribution is solid without any holes or clumping of injection points. With the randomly distributed injection points, there are areas with no injectors along with clumps which could either over- or under-predict deposition depending on where these irregularities occur. Looking at Figure 4-13, it is evident that a clump or hole of particle injectors could influence the solution.

All of these cases are run with wind normal to the inlets at moderate wind speeds. For off normal wind direction and or higher windspeeds, more verification could be required for using the 25.2pts/m^2 in a grid. To ensure that this recommended distribution of injection points is still valid, run the case with 252.0pts/m^2 in a presentation grid to ensure that 25.2pts/m^2 still produces an accurate solution.

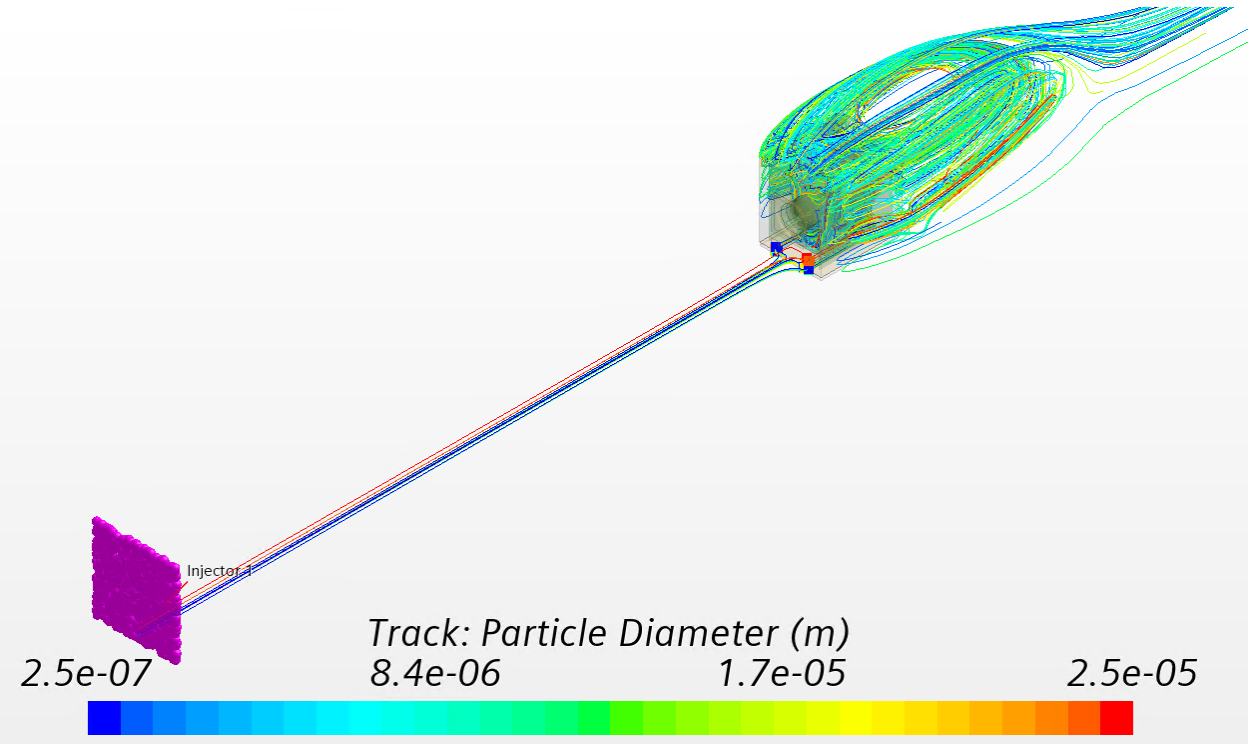

Figure 4-13. Particle Tracks Entering the Cask

4.5.2 Three AHSM-HS Wind Effects Model

A velocity, normal to the AHSM-HS inlets, of 1.5 m/s was run with the three AHSM-HS wind effects model. The particles were injected near the boundary of the external environment directly upstream of the AHSM-HS inlets with a table injector that included 2556 injector points. The model was run with both the 2019 and 2021 particle deposition models and results are shown in Table 4-9. The results show that less than 2% of the particles that are injected at the external boundary enter the three AHSM-HS modules. Figure 4-14 plots the particles entering the AHSM-HS inlets. For this low wind condition, more particles enter the high heat and low heat modules than the no heat module. These results are preliminary.

Table 4-9. Efficiency of Particles Entering the Inlets for the Three AHSM-HS Wind Effects Model

Model	Total Heat Load [kW]	Wind Speed [m/s]	Total Efficiency into AHSMs	Particles into AHSM-HS Efficiency		
				High Heat Canister	No Heat Canister	Low Heat Canister
3 AHSM-HS Wind Effects with 2019 Particle Model	50	1.5	1.54%	0.64%	0.37%	0.53%
3 AHSM-HS Wind Effects with 2021 Particle Model	50	1.5	1.37%	0.59%	0.33%	0.45%

1. Particles into AHSM-HS efficiency represents the fraction of particle mass entering the inlets versus the total particle mass injected near the external environment boundary.

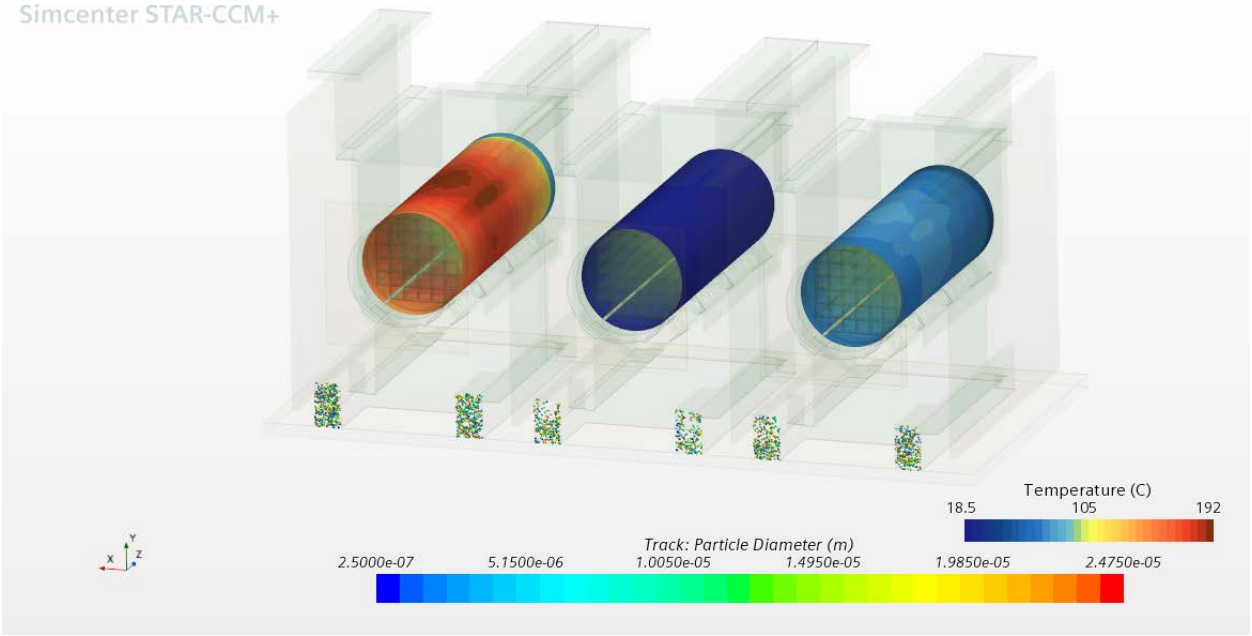

Figure 4-14. Particles Entering the Inlets of the Three AHSM-HS Wind Effects Model. The External DSC Shell Temperatures are Also Plotted

The standalone three AHSM-HS deposition model was run using the average inlet velocities calculated from the wind effects model with a 1.5 m/s velocity normal to the inlets. The particle mass injected at each of the inlets of the standalone model was taken from the particle mass entering the inlets for each AHSM-HS in the wind effects model. In the standalone model the particle mass for each module was distributed over approximately 2000 surface injectors per AHSM-HS. Table 4-10 compares the canister deposition predicted by both the wind effects and standalone model. The canister deposition is plotted for both models in Figure 4-15. The results show that the wind effects model under predicts the deposition for the heated canisters. This is most likely due to the difference of injector resolution within the AHSMs, which is apparent in the plot comparisons in Figure 4-15. The standalone model spreads the particle mass entering the inlets over significantly more injectors than the wind effects model where only a small number of particle injector trajectories make it to the AHSM-HS inlets. It is important to note that the

goal of the wind effects model is to determine how many particles make it into the AHSMs. This information could then be fed into the standalone model and a more accurate prediction of canister deposition provided.

Table 4-10. Comparison of Canister Deposition Efficiency for Three AHSM-HS Deposition Models – PRELIMINARY

Model	Total Heat Load [kW]	Wind Speed [m/s]	Canister Deposition Efficiency[1]		
			High Heat Canister	No Heat Canister	Low Heat Canister
3 AHSM-HS Wind Effects with 2021 Particle Model	50	1.5	6.28%	7.18%	9.48%
3 AHSM-HS Standalone with 2021 Particle Model	50	1.5	9.53%	7.10%	11.08%

1. Deposition efficiency represents the fraction of particle mass deposited on surfaces versus the total particle mass injected at the inlets.

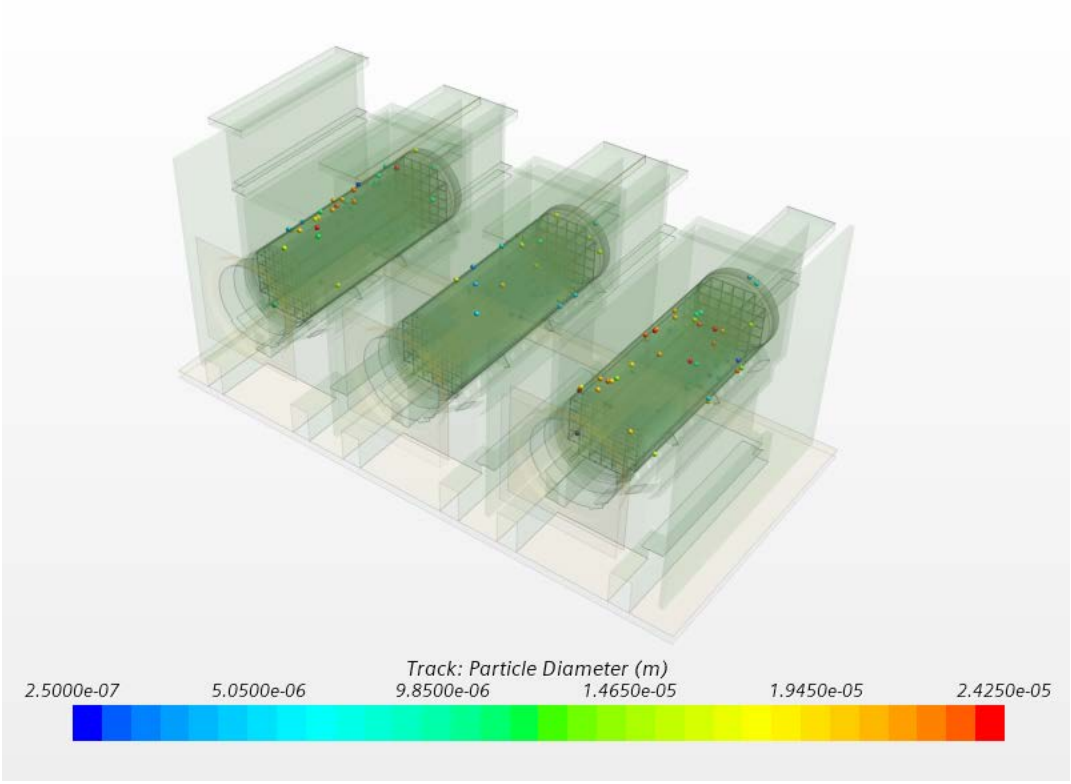

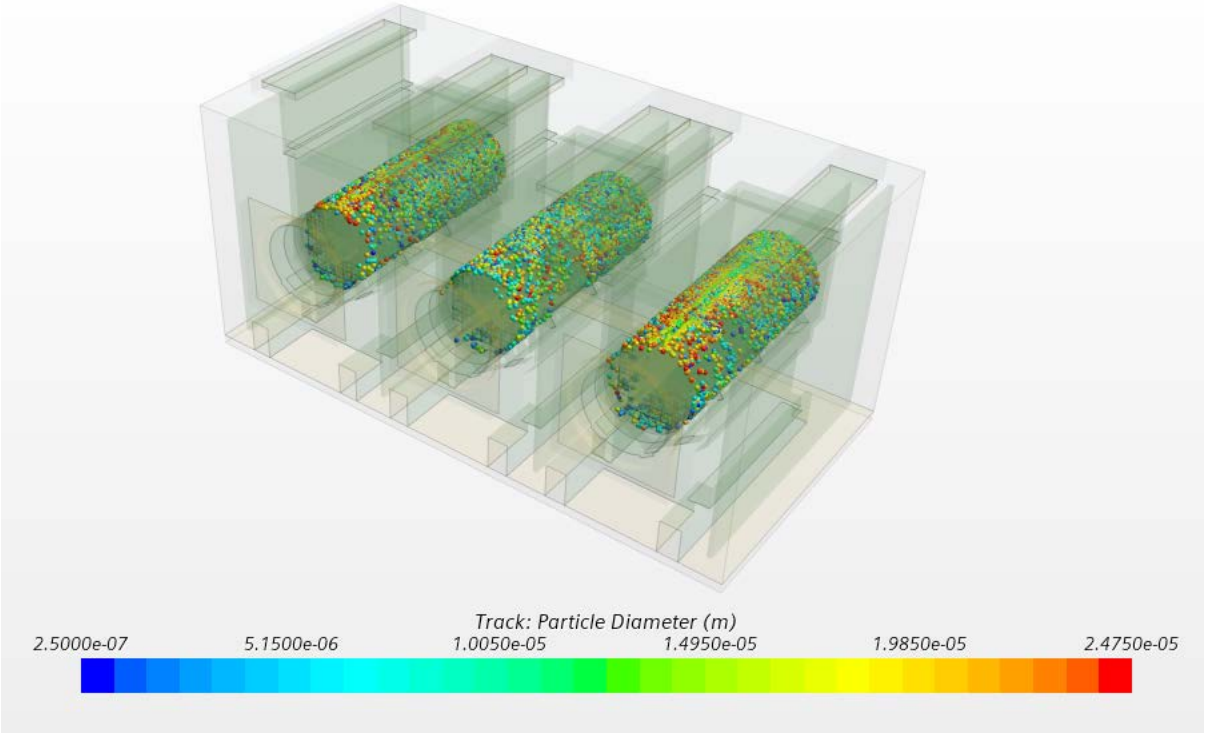

Figure 4-15. Canister Deposition Plots of Three AHSM-HS Models with 1.5 m/s Velocities Normal to Inlets for (a) Wind Effects Model and (b) Standalone Model

4.6 Droplet Composition and Size Variability due to Relative Humidity

The current 2021 particle deposition model in STAR-CCM+ does not include droplet evaporation. PNNL has looked at droplet evaporation validation cases with STAR-CCM+ and the results are documented in Jensen et al. (2020b). Future work will incorporate the droplet evaporation model into the STAR-CCM+ deposition model and the AHSM-HS model for the CDFD project. As a particle flows through a storage overpack with a heated DSC the droplet composition and size will change. Using the following approach, particle size and composition of sea-salt aerosols (SSA) will be determined for use in the deposition model.

During inland transport, SSAs undergo aging processes that alter the particle composition (e.g., evaporation) and size. Using data described in Tang et al. (1997) and an approach developed by Zhang (2005) the SSA solute weight fraction is calculated as a function of local relative humidity (RH) conditions. The correction is independent of particle size and is applied to the particle distribution used in the model. This simple method for correcting SSA particle composition is applicable over a wide range of RH (0.45-0.99) and closely matches experimental and modeled data.

4.7 Site Model

A site model provides a way to estimate air movement in and around dry cask storage systems. It should also estimate particulate (dust, sea spray, etc.) deposition on and around dry cask storage systems. Site model simulation results can also inform smaller scale simulations of storage systems or groups of storage systems, with boundary conditions, droplet, and particle fluxes. This information might be in the form of a time series, driven by observed meteorology. Or, it could be a finite, or steady state, set of "predominate" conditions driven by summarized meteorological conditions.

In this section, a candidate simulation code is identified. To illustrate the code's use and likely products, it was applied to an imaginary SNF storage facility site. Some example simulations were performed to show the code's utility for estimating site air movement, particulate deposition, and thermal effects of SNF storage structures.

4.7.1 Fire Dynamics Simulator

The Fire Dynamics Simulator (FDS) ([McGrattan et al., 2013]) is a CFD code that was originally developed to simulates low Mach number air flows and the effects of combustion on those flows. FDS is developed and maintained by the U.S. National Institute of Standards and Technology (NIST). The primary FDS application space has included thermally driven flows within buildings, design of fire suppression systems, and forensic analysis of historic building fires. Over the past decade, the FDS application space has expanded to include outdoor air flow and fire, including wildfire and pollutant dispersion. These capabilities also have applicability to simulations of stored ISFSI environments at the site scale. A more detailed account of FDS history and capability is presented by NIST (2018).

FDS uses the large eddy simulation (LES) method for air phase simulation. Relative to RANS, LES preserves larger, transient, turbulent flow structures given sufficient mesh resolution. Such turbulent structures can be significant, particularly to the dispersion of Lagrangian particles. FDS also simulates thermal energy transport and the effect of thermal gradients and radiation on the flow field. While the transport of thermal (long wave) radiation is represented in FDS, external solar (short wave) radiation is not. Full conjugate heat transfer within 3D objects is also an option but was in beta testing at the time of writing. FDS can simulate the fate of suspended liquid or solid Lagrangian particles within the simulated flow field. This includes turbulent dispersion and evaporation/condensation of liquid droplets. Liquid

droplets can also be re-suspended after deposition on solid objects. Full theoretical documentation of these capabilities can be found in McGrattan et al. (2017).

FDS uses a Cartesian rectilinear mesh. This has some advantages in that such a mesh is relatively easy to specify. Intricate mesh generation methods required by boundary-fitted polygonal meshes, as used by Star-CCM, are not required. FDS represents arbitrarily shaped solids by internally dividing rectilinear cells into polygons where immersed solid boundaries exist (cut cells). This feature may be relatively new to FDS and is not fully documented (see McGrattan et al., 2017, § 12), but has been relatively robust in the simulations performed here. In some ways, this approach is also a disadvantage, particularly in boundary layer flow representation.

The FDS code can use the Message Passing Interface [MPI] (Gropp et al., 2009). This allows FDS use on high performance distributed memory computers to reduce run time by orders of magnitude. Some FDS simulations, as part of this work, have utilized upwards of 1200 processors simultaneously.

4.7.2 Example Site Geometry

A simple geometry was prepared to exercise FDS (Figure 4-16). The geometry depicts a hypothetical ISFSI site. The terrain is that of a coastal location, where the site is near and somewhat elevated from the water (blue in Figure 4-16) and rises moderately away from shore to 70 m above the water. The site itself includes a reactor building (pink in Figure 4-16), and an adjacent storage pad (black) where some horizontal storage modules are arrayed (also pink). The buildings stand in a shallow depression excavated from the surrounding terrain.

The domain is 900 by 900 m horizontally (2950 by 2950 ft), in which the site is centered, and 240 m (790 ft) high. The domain was sized so that at least a 200 m (660 ft) fetch surrounds the site in all directions. This is sufficient to fully develop a wind profile from the domain boundary in any direction.

In the example simulations described below, the domain was divided into 2x2x2 m (6.5x6.5x6.5 ft) cells in 162 mesh blocks. Simulations were performed on PNNL’s Research Computing supercomputer.

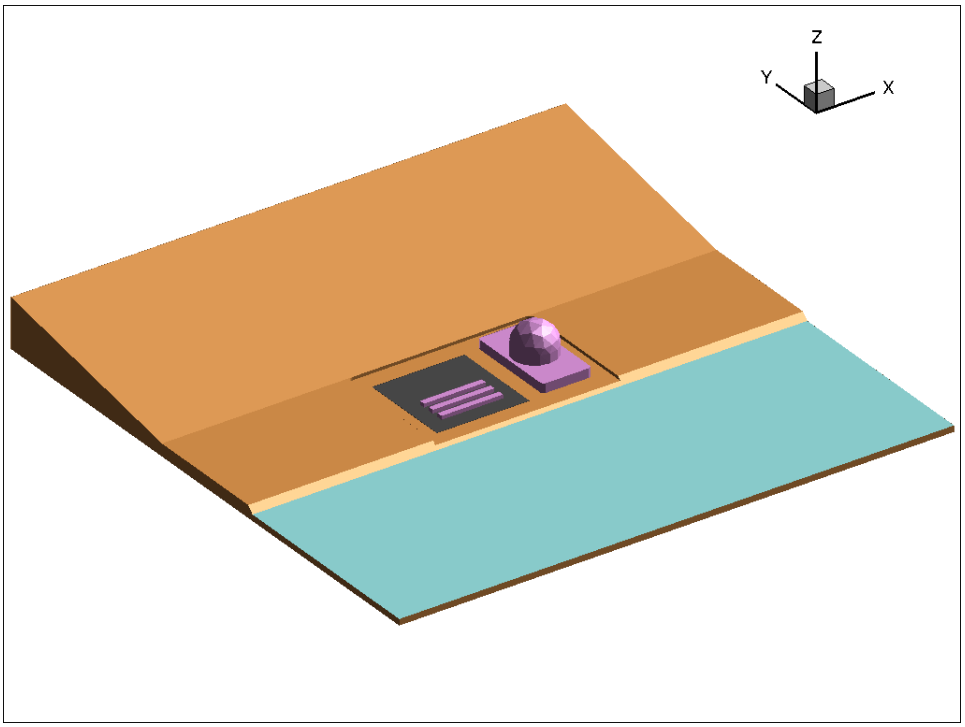

Figure 4-16. Simple Geometry Representing a Hypothetical Coastal Site Used To Exercise Fire Dynamics Simulator

4.7.3 Flow Simulation

A simple flow field simulation was prepared using the example geometry. In this flow case, an ambient wind speed of 5.0 m/s (16 ft/s) and an azimuth varying from 270° (parallel to shore) through 180° (directly onshore flow) to 90° (parallel to shore in the opposite direction). Figures 4-17, 4-18, and 4-19 show instantaneous simulated flow fields for the three ambient wind azimuths. Each figure shows constant Z and X slices through the fictitious SNF storage area. Vectors shown in the figures are parallel to the slices. Even with this rather simple geometry, the simulated flow fields in and around the SNF storage structures are quite complex.

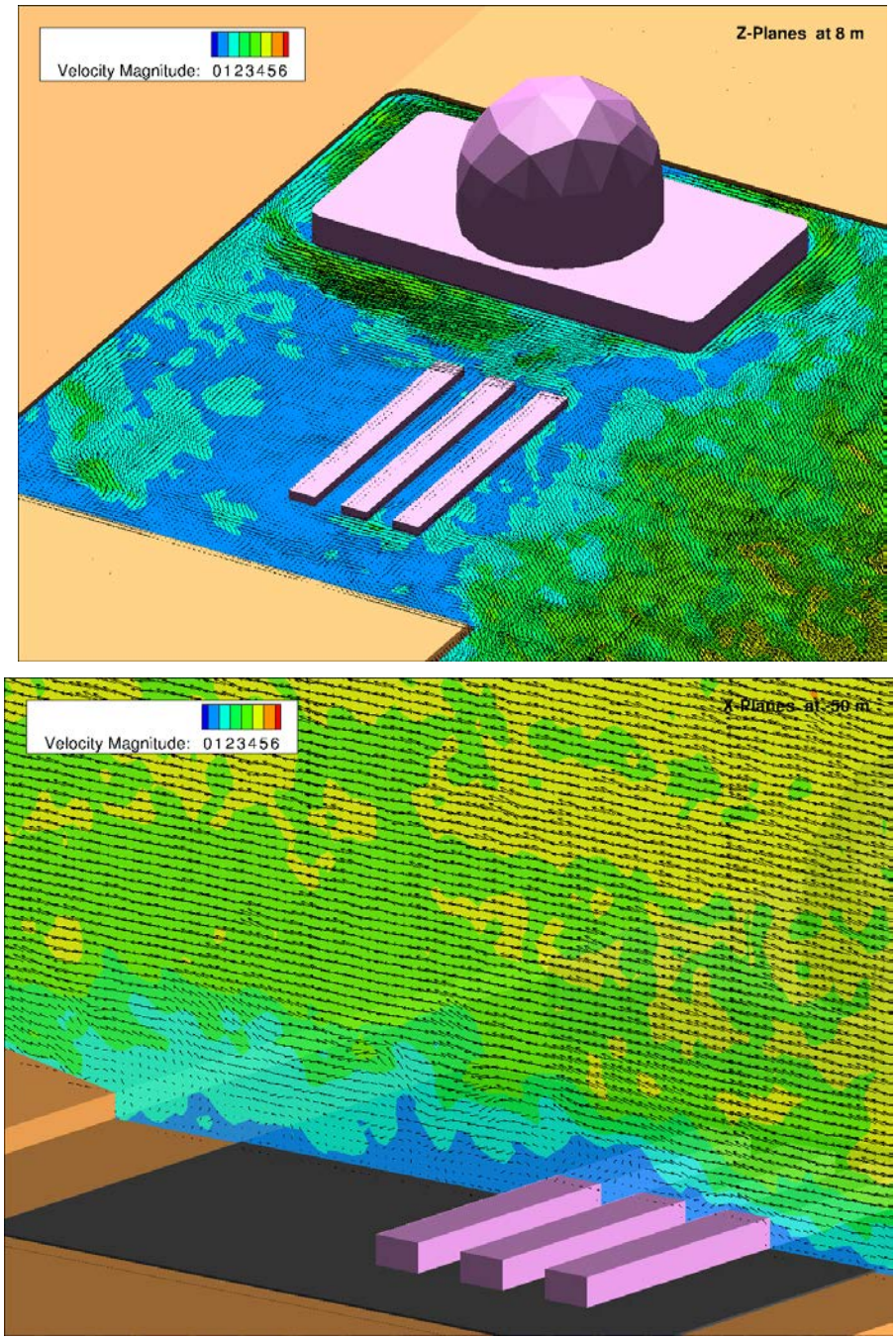

Figure 4-17. Constant Z (above) and X (below) slices Through the Simulated Flow Field Within a Hypothetical Site with the Ambient Wind Azimuth Of 210°. Velocity Vectors (in m/s) are Parallel to the Slice

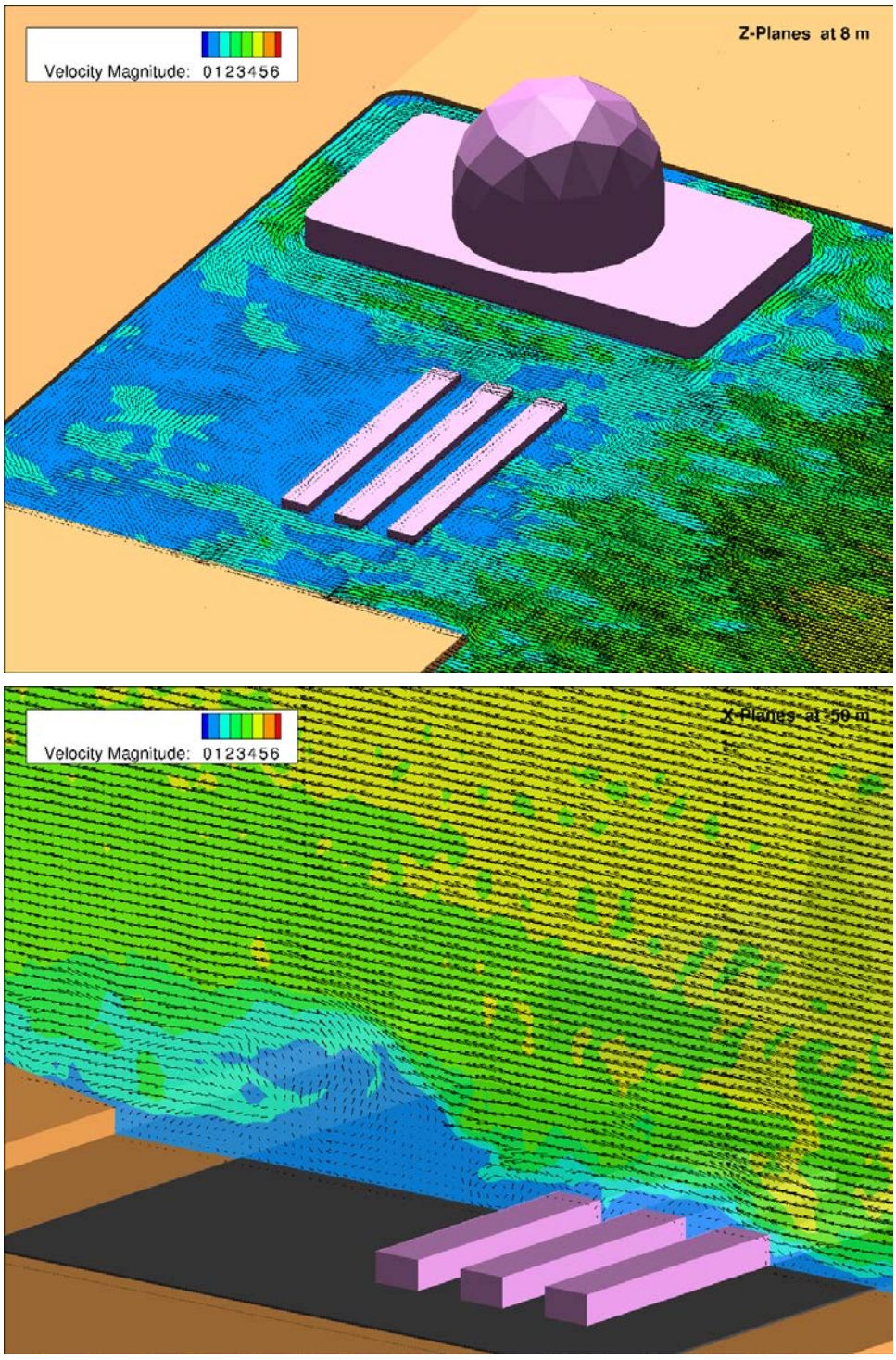

Figure 4-18. Constant Z (above) and X (below) Slices Through the Simulated Flow Field Within a Hypothetical Site with the Ambient Wind Azimuth of 180° (directly onshore). Velocity Vectors (in m/s) are Parallel to the Slice

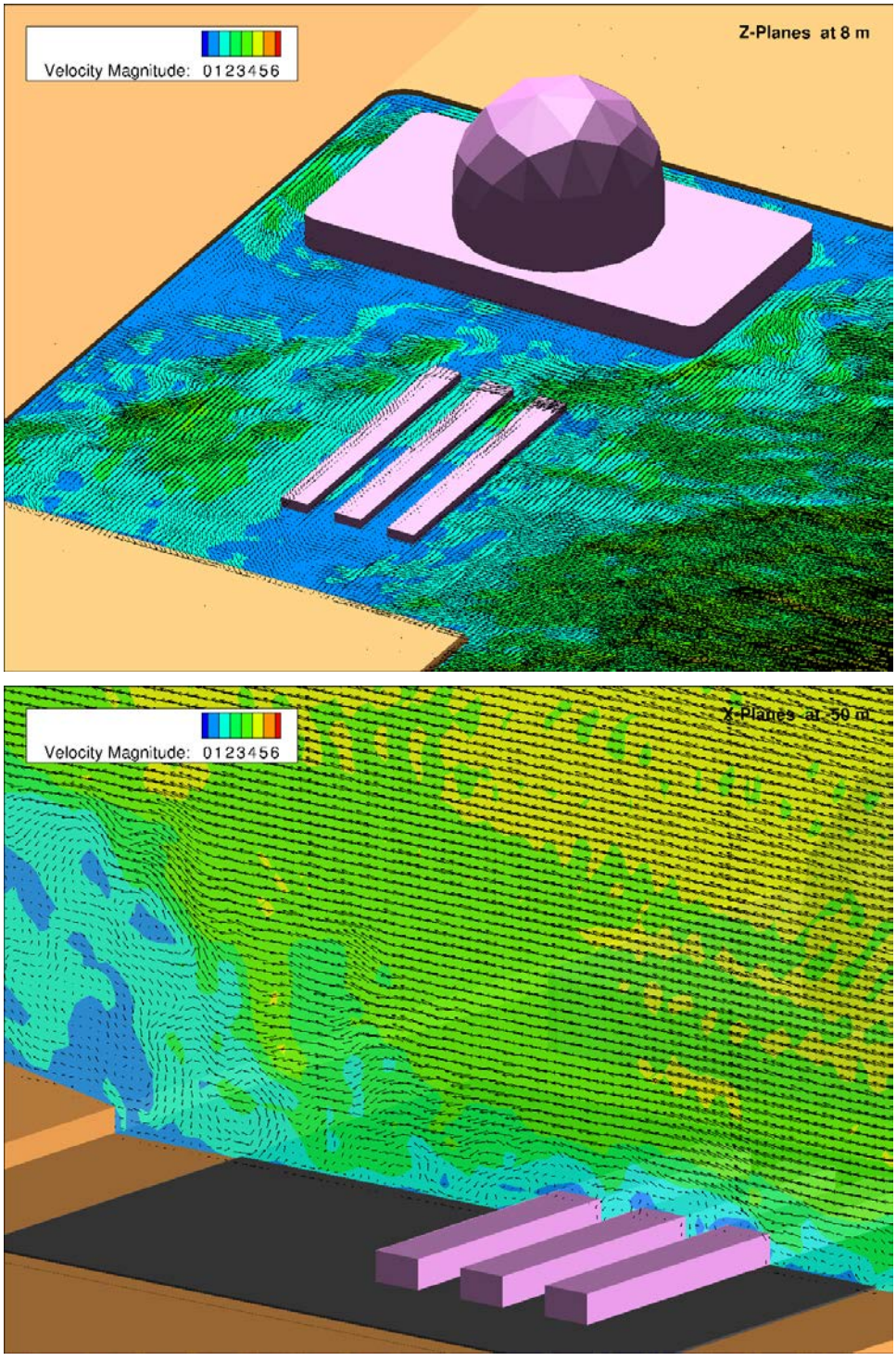

Figure 4-19. Constant Z (above) and X (below) Slices Through the Simulated Flow Field Within a Hypothetical Site with the Ambient Wind Azimuth of 150°. Velocity Vectors (in m/s) are Parallel to the Slice

4.7.4 Sea Spray Deposition

A simulation was set up to demonstrate the simulation of water droplets in and around the imaginary generation site. A directly onshore (180°azimuth) flow of 5.0 m/s (16 ft/s) was imposed. This flow was allowed to develop for a short time. Afterward, a constant mass flux of water droplets, representing sea spray, were randomly injected within a volume over the "surf zone" for a short time. The water droplet sizes were uniformly distributed from 0.25 to 25.0 μm. Figure 4-20 shows all simulated droplet tracks, the large majority of which were transported out of the model domain. Figure 4-21 shows where droplets were deposited during the simulation and their tracks prior to deposition.

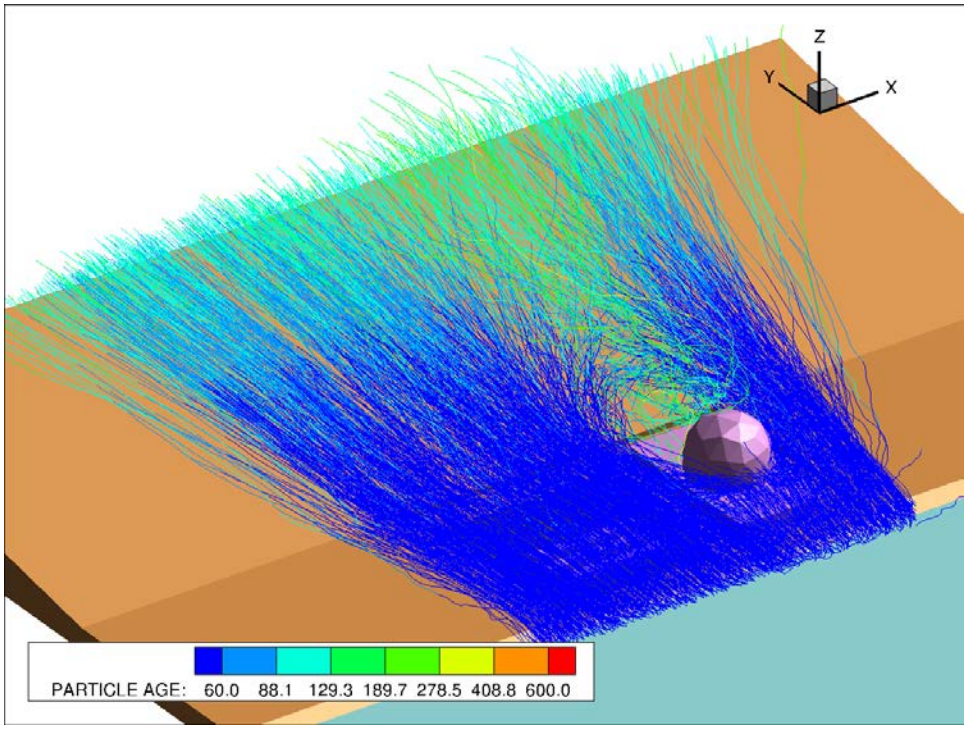

Figure 4-20. Tracks of Simulated Droplets Over the Fictitious Nuclear Generator Site. Particle Age is in Seconds

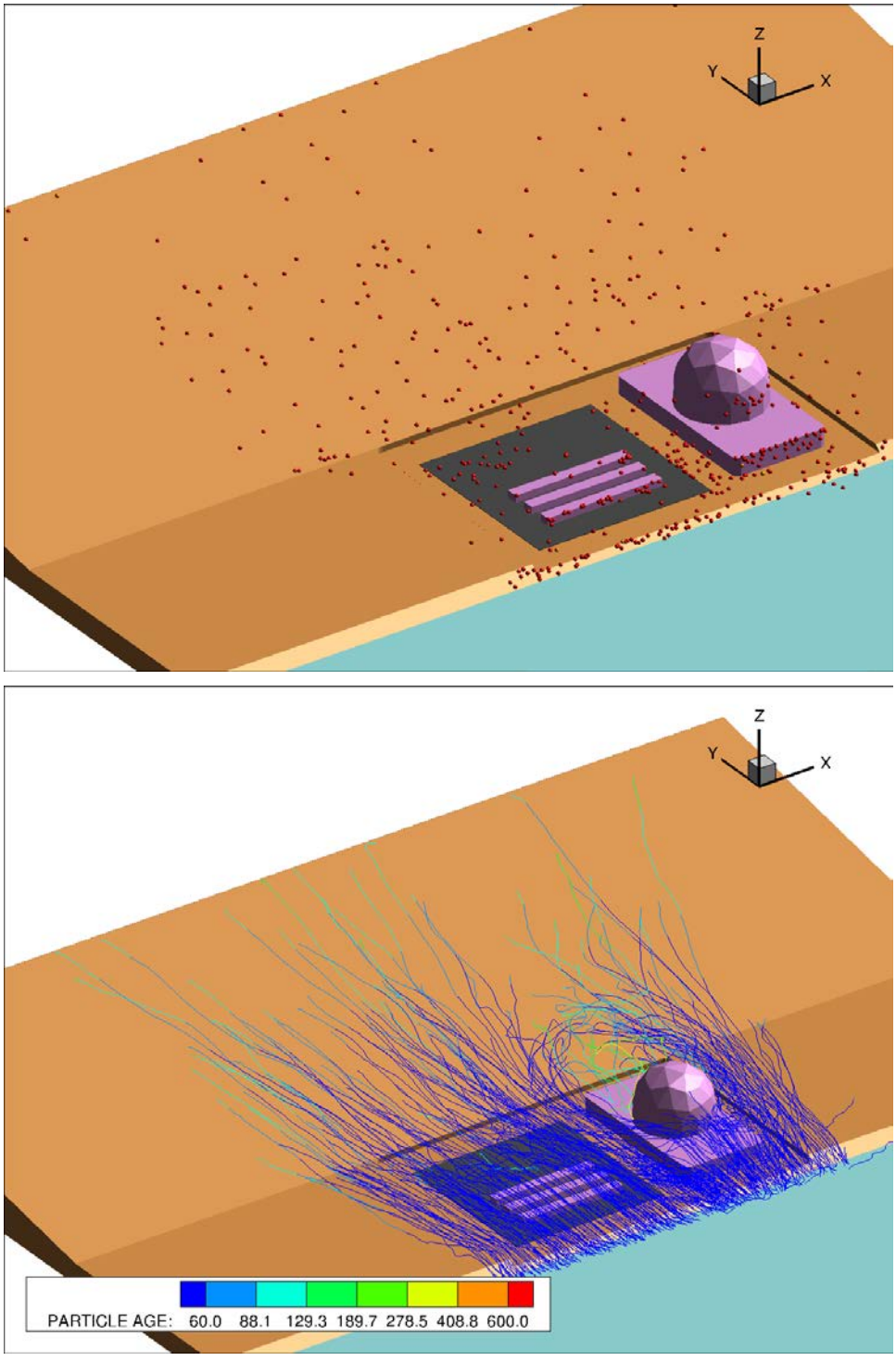

Figure 4-21. Locations Where Simulated Droplets Landed (Above) and the Tracks of Those Droplets (Below). Particle Age is in Seconds

4.7.5 Thermal Simulation

As pointed out above, FDS can simulate thermal effects on the flow field. To illustrate, a simulation was prepared similar to that in Section 4.7.4, but with an onshore flow (180°azimuth) of only 1.0 m/s (3.3 ft/s). The ambient temperature was set to 10°C (50°F). The roofs of the imaginary SNF storage structures were assigned a 2.5 kW/m^2 heat emission. This was the only assigned thermal boundary condition, meaning all other solid surfaces were at the ambient temperature. Figure 4-22 shows constant X slices through the flow solution instant. The thermal plume from the imaginary SNF structures dominate the air flow in otherwise calm conditions. Admittedly, this would probably be an extreme case in reality, but it may be that SNF heat effluents may have a significant impact on local air flow.

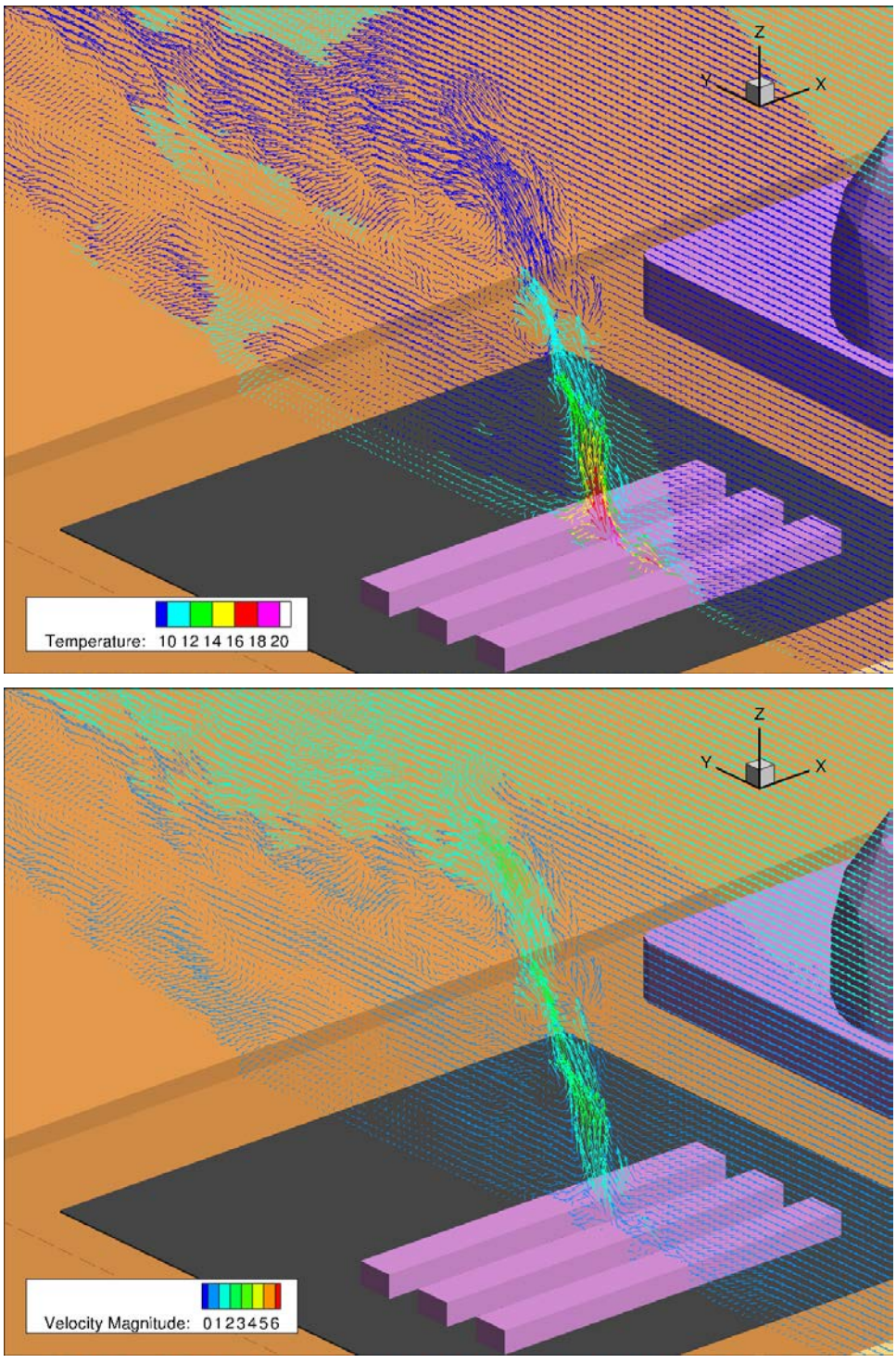

Figure 4-22. Simulated Velocity Over Imaginary SNF Storage Structures Emitting a Thermal Plume. Above and Below Show the Same Velocity Vectors Along a Constant X Slice. The Vectors are Colored by Temperature (in °C) Above and Velocity Magnitude (in m/s) Below

4.7.6 Application Strategy

The simulations discussed above cannot provide quantitative information for any actual site, but they are helpful by illustrating how FDS may be applied to a site in order to derive quantitative information. By modeling this hypothetical site data requirements for model setup can be identified. Additionally, a strategy for calibration and validation can be developed, including on-site observations needed.

The primary data requirements are geometry and ambient meteorological conditions. An accurate geometry is key, including surrounding terrain, site buildings, and other significant obstructions. Additionally, some delineation of surface material should be included (asphalt, bare ground, concrete, etc.), so appropriate surface roughness can be assigned. It would probably be best if ambient meteorology (wind speed and direction, temperature, and humidity) is derived from on-site or very nearby observations.

For a coastal site, as depicted here, some approximation of sea spray mass flux and droplet size distribution is necessary. These are functions of the surf zone size and meteorologic conditions (e.g., Eijk et al., 2011; Jensen et al., 2016).

A thermal simulation will require an accurate depiction of heat fluxes from existing stored SNF on-site, if any. Some representation of atmospheric and solar driven diurnal heating and cooling of the various surfaces, e.g., pavement, structures, and water, may also be necessary. FDS cannot simulate this directly, but a series of such surface temperatures could be estimated (e.g., Herb et al., 2008) and assigned as boundary conditions.

Calibration and validation simulations could be relatively short, transient simulations, on the order of a few days to a week. Experience with the simulations presented here and others with a real site indicate simulation of such a time frame at appropriate resolution is tractable. The primary calibration goal would be to match on-site wind speed and temperature observations (observations independent of those used to establish ambient conditions). The main parameters adjusted will be those for the ambient wind profile shape and stability.

Any application of FDS will require a mesh independence study. This involves repeated simulations at increasingly small resolutions, while monitoring simulated velocity and temperature at discrete locations. When a change in resolution no longer affects simulated velocity and temperature, the simulation is considered mesh independent. A similar kind of test should also be performed to determine the minimum number of droplets needed to simulate consistent fluxes at discrete locations.

This page is intentionally left blank.

5. CONCLUSIONS AND RECOMMENDATIONS

Thermal and deposition models have been constructed for the CDFD project. These models are preliminary, and development of the models will continue. Thermal modeling was used to help SNL design an electrical heater that will replace the SNF assemblies in the 32PTH2 canisters and provide prototypic canister temperatures. The thermal modeling was also used to help in the design of an intermediate wall with embedded insulation to thermally isolate the AHSM-HS modules from each other. The model predicts that the intermediate wall will adequately isolate the no heat AHSM-HS from the neighboring high and low heat AHSMs. The no heat canister will act as a control canister and limiting thermal loadings to this module will allow deposition to be mainly driven by wind effects.

The deposition models were updated to include turbulent dispersion particle forces, which significantly increases deposition predictions along the canister surface. Significant progress has also been made to create a site model to understand particle flow and distribution at an ISFSI. Since no site has been selected for the CDFD project at this time a generic coastal site was considered for the report. Future development of the deposition models will include adding particle evaporation. Adding particle re-suspension will also be explored in future model development. The PNNL deposition models have not been validated, and though the CDFD project will help validate the models, additional experimental data and modeling studies are recommended for the development of the deposition modeling.

To continue development of the thermal and deposition models the following activities are recommended:

- Update AHSM-HS models with canister test model changes, including basket properties and surface emissivities.
- Update AHSM-HS models with electrical heaters to replace the SNF assemblies once a heater design has been finalized.
- Further investigation of backflow conditions due to wind speed and directions, and the impact of backflow.
- Simulate transient environmental boundary conditions, including ambient temperature, solar loadings, and wind.
- Add droplet evaporation into the STAR-CCM+ deposition model. This will also include re-evaluating the deposition efficiency calculation with changing particle size and mass.
- Explore adding particle re-suspension to the deposition models.
- Validate the deposition model with benchtop testing.

This page is intentionally left blank.

6. REFERENCES

10 CFR 71. "Packaging and Transportation of Radioactive Material," *Code of Federal Regulations*, January 2020.

Andersson B, R Andersson, L Hakansson, M Mortensen, R Sudiyo, and B van Wachem. 2012. *Computational Fluid Dynamics for Engineers*. Cambridge University Press, New York.

Dassault Systemes SolidWorks Corp. 2020. SolidWorks Premium 2020 (computer software). Waltham, Massachusetts: Dassault Systemes.

Eijk AMJv, JT Kusmierczyk-Michulec, MJ Francius, G Tedeschi, J Piazzola, DL Merritt, and JD Fontana. 2011. "Sea-spray aerosol particles generated in the surf zone." *Journal of Geophysical Research: Atmospheres* 116 (D19).

Electric Power Research Institute. 2015. "Susceptibility Assessment Criteria for Chloride-Induced Stress Corrosion Cracking (CISCC) of Welded Stainless Steel Canisters for Dry Cask Storage Systems". EPRI Report No 3002005371.

Fort JA, DJ Richmond, JM Cuta, and SR Suffield. 2019. *Thermal Modeling of the TN-32B Cask for the High Burnup Spent Fuel Data Project*. PNNL-28915, Pacific National Laboratories, Richland, Washington.

Gropp W, R Graham, A Moody, T Hoefler, R Treumann, J Träff, G Bosilca, D Solt, B de Supinski, R Thakur, et al.. 2009. "MPI: A message-passing interface standard version 2.2." In *Message Passing Interface Forum*, Vol. 5, pp. 32–43.

Herb WR, B Janke, O Mohseni, and HG Stefan. 2008. "Ground surface temperature simulation for different land covers." *Journal of Hydrology* 356(3):327–343.

Holman, J. 1997. *Heat Transfer*. New York: McGraw-Hill.

Jensen PJ, T Tran, BG Fritz, FC Rutz, SB Ross, AM Gorton, R Devanathan, P Plante, and K Trainor 2016. "Preliminary Evaluation of the DUSTRAN Modeling Suite for Modeling Atmospheric Chloride Transport." Air Quality Atmosphere and Health, May 2016, doi:10.1007/s11869-016-0404-5

Jensen PJ, T Tran, BG Fritz, FC Rutz, SB Ross, AM Gorton, R Devanathan, P Plante, and K Trainor 2016. "Preliminary Evaluation of the DUSTRAN Modeling Suite for Modeling Atmospheric Chloride Transport." Air Quality Atmosphere and Health, May 2016, doi:10.1007/s11869-016-0404-5.

Jensen PJ, SR Suffield, CL Grant, CJ Spits, and JT Simmons. 2020a. *Preliminary Deposition Modeling: For Determining the Deposition of Corrosive Contaminants on SNF Canisters*. PNNL-29620. Pacific Northwest National Laboratory, Richland, Washington.

Jensen PJ, SR Suffield, and BJ Jensen. 2020b. *Status Update: Deposition Modeling For SNF Canister CISCC*. PNNL-30793. Pacific Northwest National Laboratory, Richland, Washington.

Lindgren ER, SG Durbin, SR Suffield, and JA Fort. 2021. *Status Update for the Canister Deposition Field Demonstration.* SAND2021-6471, Sandia National Laboratories, Albuquerque, New Mexico.

Liu B and JK Agarwal. 1974. *Experimental Observation of Aerosol Deposition in Turbulent Flow*. Aerosol Science, 1974, Vol. 5. pp. 145-155.

Mcgrattan KB, RJ McDermott, CG Weinschenk, GP Forney. 2013. *Fire Dynamics Simulator, Technical Reference Guide*, Sixth Edition. Special Publication (NIST SP), National Institute of Standards and Technology, Gaithersburg, MD, [online], https://doi.org/10.6028/NIST.sp.1018 (Accessed July 21, 2021) https://www.nist.gov/publications/fire-dynamics-simulator-technical-reference-guide-sixth-edition

McGrattan K, R McDermott, C Weinschenk, and K Overholt. 2017. *Fire Dynamics Simulator; Technical Reference Guide, Volume 1: Mathematical Model*. Special Publication (NIST SP) 1018-1, National Institute of Standards and Technology, Gaithersburg, MD.

Menter FR. *Two-equation eddy-viscosity turbulence models for engineering applications*, AIAA J. 32 (1994) 1598–1605, https://doi.org/10.2514/3.12149.

Saffman, P. 1965. *The Lift on a Small Sphere in a Slow Shear Flow*. Journal of Fluid Mechanics 22 (1965): 385-400.

Shih TH, WW Liou, A Shabbir, Z Yang, and J Zhu. *A new kappa-epsilon eddy viscosity model for high Reynolds number turbulent flows*, Comput. Fluids 24 (1995) 227–238, https://doi.org/10.1007/978-3-319-27386-0_7.

Siemens PLM Software. 2021. STAR-CCM+ 16.02 (computer software). Plano, Texas: Siemens PLM Software.

Siemens. *External Aerodynamics with Simcenter STAR-CCM+*. Siemens Digital Industries Software. 2020a.

Siemens. *Best Practices: External Aerodynamics for Aerospace Applications.* Siemens Digital Industries Software. 2020b.

Siemens. *How should the initial and boundary conditions for pressure be set when gravity is enabled on a compressible ideal gas?*. Siemens Digital Industries Software. 2018. https://support.sw.siemens.com/en-US

Suffield SR, DJ Richmond, and JA Fort. 2019. *Modeling of the of the Boiling Water Reactor Dry Cask Simulator*. PNNL-28424, Pacific National Laboratories, Richland, Washington.

Suffield SR, DJ Richmond, BJ Jensen, JA Fort and C Grant. 2020. *Modeling of the of the Horizontal Boiling Water Reactor Dry Cask Simulator*. PNNL-30145, Pacific National Laboratories, Richland, Washington.

Tang IN, AC Tridico, and KH Fung. 1997. *Thermodynamic and optical properties of sea salt aerosols*. Journal of Geophysical Research Atmospheres. October 1997, Vol. 102, Issue D19, pp. 23269-23275.

Tang Y and B Guo. 2011. *Computational fluid dynamics simulation of aerosol transport and deposition*. Frontiers of Environmental Science & Engineering in China. 2011, 5(3): 362-377.

Wang Y and PW James. 1999. *On the effect of anisotropy on the turbulent dispersion and deposition of small particles.* International Journal of Multiphase Flow 25 (1999) 551-558.

UFSAR. 2011. "Public Versions of Standardized Advanced NUHOMS® System UFSAR Pages and Drawings, Showing Proposed Amendment 3 Changes", ORANO/TN. NRC/ADAMS accession number ML12004A157.

United States Nuclear Regulatory Commission (NRC). 2012. *Potential Chloride-Induced Stress Corrosion Cracking of Austenitic Stainless Steel and Maintenance of Dry Cask Storage System Canisters*.

Zhang MK, EM Knipping, AS Wexler, PV Bhave, and GS Tonnesen. 2005. *Size distribution of sea-salt emissions as a function of relative humidity*. Atmospheric Environment. June 2005, Vol. 39, Issue 18, pp. 3373-3379.